



NRL/FR/7232--04-10,061

Self-shading Corrections for Oceanographic Upwelling Radiometers

ROBERT A. LEATHERS
T. VALERIE DOWNES
CURTISS O. DAVIS

*Radio, IR, Optical Sensors Branch
Remote Sensing Division*

CURTIS D. MOBLEY

*Sequoia Scientific
Bellevue, Washington*

July 6, 2004

Approved for public release; distribution is unlimited.

REPORT DOCUMENTATION PAGE				Form Approved OMB No. 0704-0188	
Public reporting burden for this collection of information is estimated to average 1 hour per response, including the time for reviewing instructions, searching existing data sources, gathering and maintaining the data needed, and completing and reviewing this collection of information. Send comments regarding this burden estimate or any other aspect of this collection of information, including suggestions for reducing this burden to Department of Defense, Washington Headquarters Services, Directorate for Information Operations and Reports (0704-0188), 1215 Jefferson Davis Highway, Suite 1204, Arlington, VA 22202-4302. Respondents should be aware that notwithstanding any other provision of law, no person shall be subject to any penalty for failing to comply with a collection of information if it does not display a currently valid OMB control number. PLEASE DO NOT RETURN YOUR FORM TO THE ABOVE ADDRESS.					
1. REPORT DATE (DD-MM-YYYY) July 6, 2004		2. REPORT TYPE Formal		3. DATES COVERED (From - To)	
4. TITLE AND SUBTITLE Self-shading Corrections for Oceanographic Upwelling Radiometers				5a. CONTRACT NUMBER	
				5b. GRANT NUMBER	
				5c. PROGRAM ELEMENT NUMBER 61153N, 602435N	
6. AUTHOR(S) Robert A. Leathers, T. Valerie Downes, Curtiss O. Davis, and Curtis D. Mobley*				5d. PROJECT NUMBER	
				5e. TASK NUMBER	
				5f. WORK UNIT NUMBER	
7. PERFORMING ORGANIZATION NAME(S) AND ADDRESS(ES) Naval Research Laboratory Washington, DC 20375-5320				8. PERFORMING ORGANIZATION REPORT NUMBER NRL/FR/7232--04-10,061	
9. SPONSORING / MONITORING AGENCY NAME(S) AND ADDRESS(ES) Office of Naval Research 800 North Quincy St. Arlington, Virginia 22217-5660				10. SPONSOR / MONITOR'S ACRONYM(S) ONR	
				11. SPONSOR / MONITOR'S REPORT NUMBER(S)	
12. DISTRIBUTION / AVAILABILITY STATEMENT Approved for public release; distribution is unlimited.					
13. SUPPLEMENTARY NOTES * Sequoia Scientific, 2700 Richards Road, Suite 107, Bellevue, Washington 98005					
14. ABSTRACT Most commercially available instruments for measuring upwelling radiance are large enough that they suffer from significant self-shading error over at least some portion of the measured spectrum. The amount of error depends on instrument dimensions, sensor FOV, water optical properties (which are wavelength-dependent), water depth, seafloor optical properties, Sun position, and atmospheric conditions. We derive analytical models for the self-shading of a buoyed or nonbuoyed radiometer in optically deep and very shallow waters. The shallow-water and deepwater models are then combined to form a complete analytical model for any water depth. We have modified a previously written Backward Monte Carlo program to numerically compute the self-shading of a buoyed or nonbuoyed radiometer. The results of these numerical simulations can be used to validate the analytical model for a particular instrument or to build a semi-analytical model. We have also written a computer program that applies self-shading corrections to upwelling radiance spectra.					
15. SUBJECT TERMS Instrument self-shading, Monte Carlo simulations					
16. SECURITY CLASSIFICATION OF:			17. LIMITATION OF ABSTRACT UL	18. NUMBER OF PAGES 55	19a. NAME OF RESPONSIBLE PERSON Robert Leathers
a. REPORT Unclassified	b. ABSTRACT Unclassified	c. THIS PAGE Unclassified			19b. TELEPHONE NUMBER (include area code) 202-767-6504

CONTENTS

1. INTRODUCTION	1
2. ANALYTICAL APPROXIMATIONS	8
2.1 Sensor Self-shading in Deep Water	8
2.2 Buoy Shading in Deep Water	11
2.3 Putting it Together: Self-shading of Buoyed Radiometers in Deep Water	13
2.4 Self-shading in Shallow Water: Infinitesimal FOV	16
2.5 Self-shading in Shallow Water: Finite FOV	17
3. MONTE CARLO SIMULATIONS	26
3.1 The Modified BMC3D Code	26
3.2 Ray-tracing Data Tables	30
3.3 Post-processing of the Ray-Tracing Results	31
3.4 Results for a Non-buoyed Radiometer	33
3.5 Results for the Hyper-TSRB in Deep Water	35
3.6 Results for the Hyper-TSRB in Shallow Water	41
4. RADIOMETER DATA CORRECTION	44
4.1 Correction Algorithm	44
4.2 Field Data Examples	46
5. CONCLUSIONS	48
6. ACKNOWLEDGMENTS	49
REFERENCES	49

SELF-SHADING CORRECTIONS FOR OCEANOGRAPHIC UPWELLING RADIOMETERS

1. INTRODUCTION

The Ocean Portable Hyperspectral Imager for Low-Light Spectroscopy (Ocean PHILLS) was designed and constructed by the Naval Research Laboratory (NRL) to image the coastal ocean [1]. Airborne optical remote sensing data were taken with the Ocean PHILLS over a region near Lee Stocking Island (LSI), Bahamas, in the summers of 1999 and 2000 [2]. The LSI deployments were part of the multi-institution Coastal Benthic Optical Properties (CoBOP) program sponsored by the U.S. Office of Naval Research (ONR) [3]. The focus of the CoBOP program was on the interaction of visible light with the water column and the seafloor in a variety of shallow-water environments. One of the goals was to develop techniques for using optical measurements, such as remote sensing reflectance from the Ocean PHILLS, to map and monitor bathymetry, water properties, sediment types, seagrass beds, and coral reefs.

Accurate sea-truth data are vital for proper processing and analysis of the 1999 and 2000 Ocean PHILLS data and for subsequent remote sensing algorithm development. The sea-truth data should enable us to validate and refine both our sensor calibration and our atmospheric correction. In addition, much of the sea-truth taken at LSI was directly used to develop remote sensing algorithms to be applied to Ocean-PHILLS data [4-7]. The primary sea-truth for remote sensing reflectance at LSI was collected using Hyper-TSRB instruments (Satlantic Inc., Halifax, Nova Scotia, Canada). The Hyper-TSRB is a buoyed instrument that measures abovewater downwelling irradiance (E_d) and underwater upwelling radiance (L_u) at many spectral channels over the visible and near-IR range, from which remote sensing reflectance spectra can be computed. Hyper-TSRBs were deployed from small boats by the University of Miami, the University of New Hampshire, Moss Landing Marine Laboratory, and others, providing both time series and spatial transects that cover much of the LSI study area. However, the upwelling radiance sensor of the Hyper-TSRB, as with any upwelling radiometer, is subject to self-shading error.

When a radiometer is placed in water to measure upwelling light, the magnitude of the local light field is decreased by the shadow of the instrument. This effect is largest in turbid waters and at longer wavelengths [8]. Self-shading causes computed remote sensing reflectance values to be too low. Because the magnitude of the shading error is wavelength dependent, algorithms that depend on ratios of the radiance at different wavelengths to determine water optical properties [9], water constituent concentrations [10, 11], or bottom depth or features [12] will also be in error [13]. Therefore, shading corrections should be routinely applied to upwelling light measurements taken from in-water instruments. Unfortunately, instrument manufacturers do not provide self-shading correction algorithms for their products. The self-shading of various optical instruments has been investigated by Gordon and Ding [8], Zibordi and Ferrari [14], Aas and Korsbø [15], Piskozub, Weeks, Schwarz, and Robinson [16], and

Doyle [17]. However, none of these investigations dealt with a buoyed radiometer such as the Hyper-TSRB. Our need to properly correct Hyper-TSRB data motivated the work that is described in this report.

Gordon and Ding [8] provide a semianalytical model for the self-shading error of an upwelling radiance or irradiance sensor that is positioned at the end of a cylindrical housing. This model assumes that the instrument is positioned with the sensor just below the sea surface and that the water is optically deep. It is further assumed that the shading is due primarily to the bottom circular end of the instrument and that shading due to the side and top of the cylinder is insignificant. The fractional shading error is given by

$$\varepsilon = 1 - \exp(-k a r), \quad (1)$$

where a is the water beam absorption coefficient, r is the radius of the instrument housing, and k is a constant that depends on the measurement type (e.g., upwelling radiance or irradiance) and on the illumination conditions. For radiance measurements and the idealized case of a Sun in a black sky (i.e., no atmospheric scattering), the value of k is approximately equal to $2/\tan\theta_{0w}$, where θ_{0w} is the in-water solar zenith angle. Gordon and Ding [8] provide empirical values of k as derived from Monte Carlo simulations of a two-dimensional shading disk placed just below the sea surface. For convenience, these values of k for an upwelling radiance (L_u) sensor (expressed as $k \tan\theta_{0w}$) are provided in Table 1. In Table 1, a point sensor refers to a sensor of infinitesimal size, whereas a finite sensor covers the entire base of the instrument (i.e., has radius r). The values in Table 1 are for 100% collimated sunlight. Gordon and Ding's values of k for diffuse skylight are 4.61 for a point sensor and 3.74 for a finite sensor. The shading error for general sky conditions can be approximated with [8,14]

$$\varepsilon = \varepsilon_{sky} f + (1 - f) \varepsilon_{sun}, \quad (2)$$

where ε_{sun} is the shading error for direct sunlight (i.e., the value of ε from Eq. (1) using the appropriate value of k from Table 1), ε_{sky} is the shading error for skylight computed with Eq. (1) using the appropriate value of k , and f is the fraction of the total downwelling irradiance that is diffuse skylight. The ocean optics protocols for SeaWiFS validation [18] recommends the use of the Gordon-Ding model, and Zibordi and Ferrari [14] found good agreement between the Gordon-Ding model and their experimental estimates of self-shading.

Table 1 – Values of $(k \tan\theta_{0w})$ for an Upwelling Radiance (L_u) Sensor in Deep Water (from Gordon and Ding 1992)

θ_0 (deg)	$k \tan\theta_{0w}$ for a point sensor	$k \tan\theta_{0w}$ for a finite sensor
10	2.17 [*]	1.79 [*]
20	2.23 ^{**}	1.83 ^{**}
30	2.23	1.76
40	2.29	1.84
50	2.37	1.92
60	2.41	1.97
70	2.45	2.01

^{*} $ar \leq 0.01$.

^{**} $ar \leq 0.03$.

Unfortunately, for upwelling light sensors mounted in instruments that use a buoy to float on the sea surface (Fig. 1), Eq. (1) is inappropriate. Because the buoy has a larger radius than the sensor housing and is vertically separated from the sensor depth, it should be expected that the actual shading of the entire instrument in optically deep water would lie somewhere between that predicted by Eq. (1) using the radius of the sensor head and that predicted by Eq. (1) using the radius of the buoy. This range of possible values can be quite large. Equation (1) is also not valid for optically shallow waters, such as those at LSI. In optically shallow water, the instrument sees upwelling light reflected from the seafloor and from the water column, both of which are reduced by shading. The relative effects of the shading on these two components depend on the bottom reflectivity and the water quality and depth.

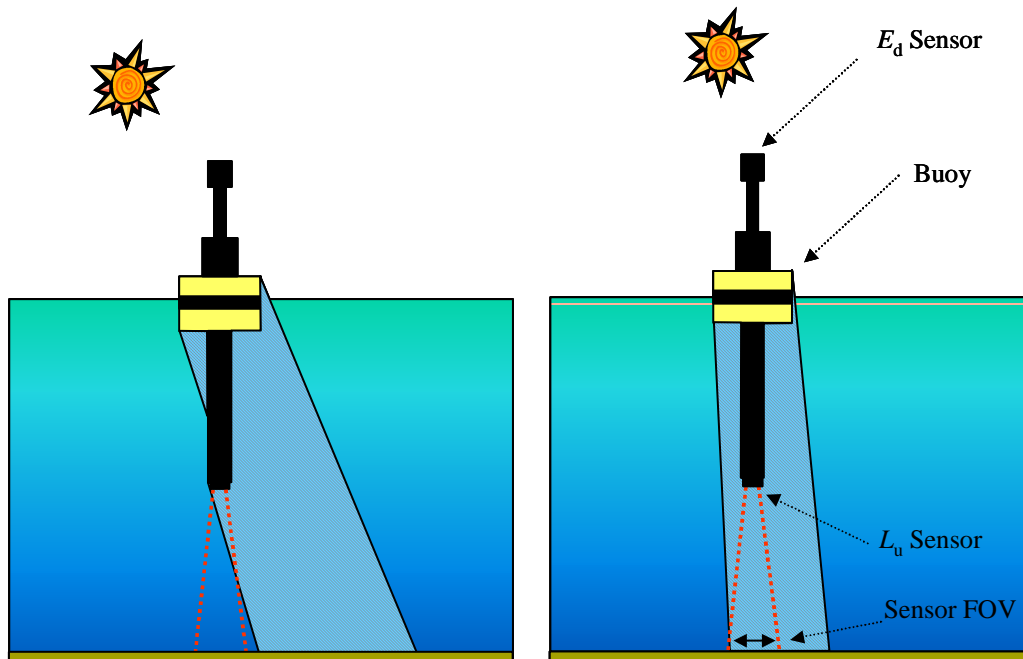


Fig. 1 — Self-shading of a buoyed radiometer. The presence of the buoy has a small effect for large solar zenith angles (left) but has a large effect for small solar zenith angles (right).

Although we cannot use Eq. (1) to accurately quantify the shading error for the Hyper-TSRB, we can use it to obtain bounds on the amount of self-shading we should expect in optically deep water. The Hyper-TSRB (Fig. 2) has been designed so that the upwelling radiance sensor is suspended 0.66 m below the sea surface. Other important dimensions for the instrument are provided in Fig. 2 and Table 2. Consider case 1 waters [19] (i.e., waters in which the optical properties are highly correlated with chlorophyll concentration [Chl]). The magnitude of the absorption coefficient $a(\lambda)$ for waters with chlorophyll concentrations of 1, 2, and 4 mg/m^3 [19] are shown in Fig. 3. The values shown for pure water ([Chl] = 0) are those measured by Pope and Fry [19, 20]. For each water absorption spectrum shown in Fig. 3, the estimated percent shading error from Eq. (1) is shown in Fig. 4 for radiance sensors with radii of 0.045 m (i.e., that of the Hyper-TSRB sensor head) and 0.15 m (i.e., that of the Hyper-TSRB buoy). The actual Hyper-TSRB self-shading in deep water should lie somewhere between these two sets of curves (i.e., for the two different radii). Results are shown both for a solar zenith angle of 20 deg and for a solar zenith angle of 40 deg. Note that the amount of shading is approximately a factor of 2 greater for $\theta_0 = 20$ deg than for $\theta_0 = 40$ deg. For either case, it can be seen that even for the clearest of waters, self-shading is important at wavelengths above 580 nm. In productive waters, such as at the LEO-15 [21] site off New Jersey, where chlorophyll concentrations often exceed 4 mg/m^3 , self-shading should be expected to be significant at all wavelengths. In fact, in waters such as those at LEO-15, there are

additional contributions to $a(\lambda)$ from dissolved organic matter and detritus (both of which absorb highly at blue wavelengths) that would further increase the self-shading error at blue wavelengths. Although we cannot draw any conclusions from Fig. 4 with regard to optically shallow waters, it is clear from this example that Hyper-TSRB self-shading is a very significant effect, especially at wavelengths over 600 nm.

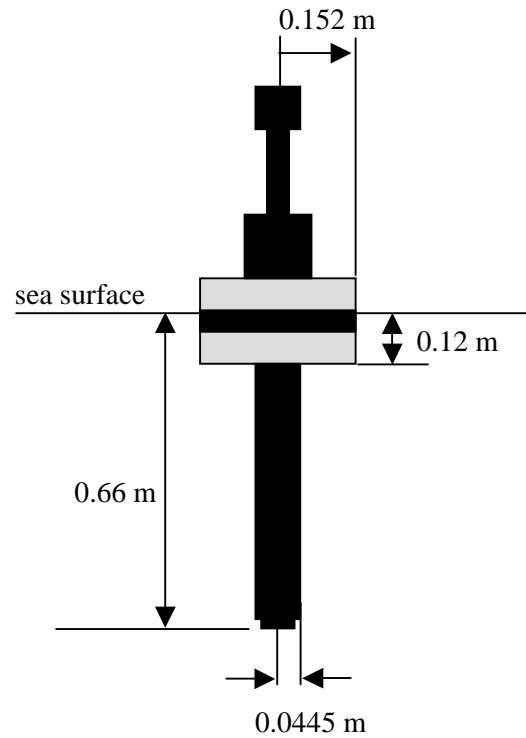


Fig. 2 — Approximate dimensions of the Hyper-TSRB

Table 2 — Hyper-TSRB Dimensions

Sensor diameter (radius)	3.50 in = 0.0889 m (0.0445 m)
Buoy diameter (radius)	12.0 in = 0.305 m (0.152 m)
Bottom of buoy to sensor	21.3 in = 0.541 m
Sensor depth	0.66 m
Buoy depth (amount of buoy underwater)	0.66 m – 0.54 m = 0.12 m

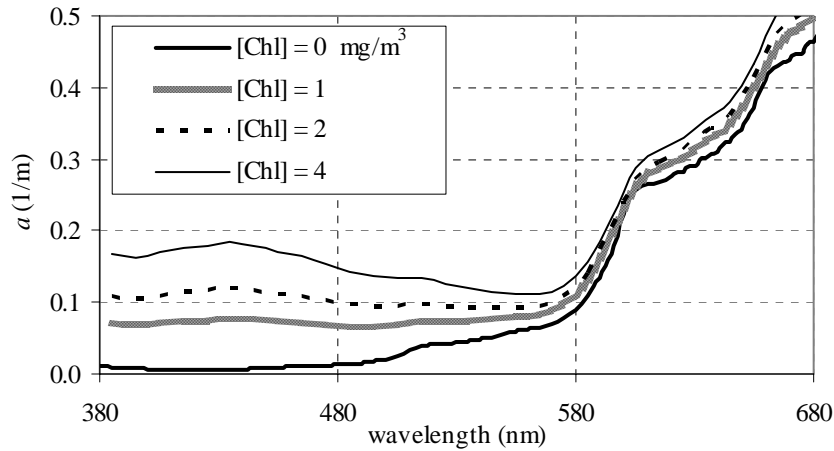


Fig. 3 — Absorption coefficient in Case 1 waters for $[Chl] = 0, 1, 2,$ and 4 mg/m^3 [19]

The purpose of the work described in this report is to accurately quantify the amount of self-shading for the Hyper-TSRB as a function of environmental conditions and to develop an algorithm for the routine correction of Hyper-TSRB data. This correction will be applied to Hyper-TSRB data from LSI to provide accurate water-leaving radiance and remote sensing reflectance. These products are used in the development and validation of algorithms for the calibration and atmospheric correction of Ocean PHILLS data taken at LSI. The analytical models and numerical tools developed to meet this task can also be applied to the dimensions of other buoyed and nonbuoyed in-water radiometers. In Section 2 we develop analytical expressions for self-shading error. In Section 3 we provide results from Monte Carlo simulations that empirically quantify the amount of self-shading for cylindrical radiometers and for the Hyper-TSRB. We use these results both to develop corrections and to evaluate our analytical models. In Section 4 we describe the computer program we developed to apply self-shading corrections to radiometer data and we show examples from LSI. A concluding summary is provided in Section 5. Descriptions of variables used throughout this report are provided here in Table 3.

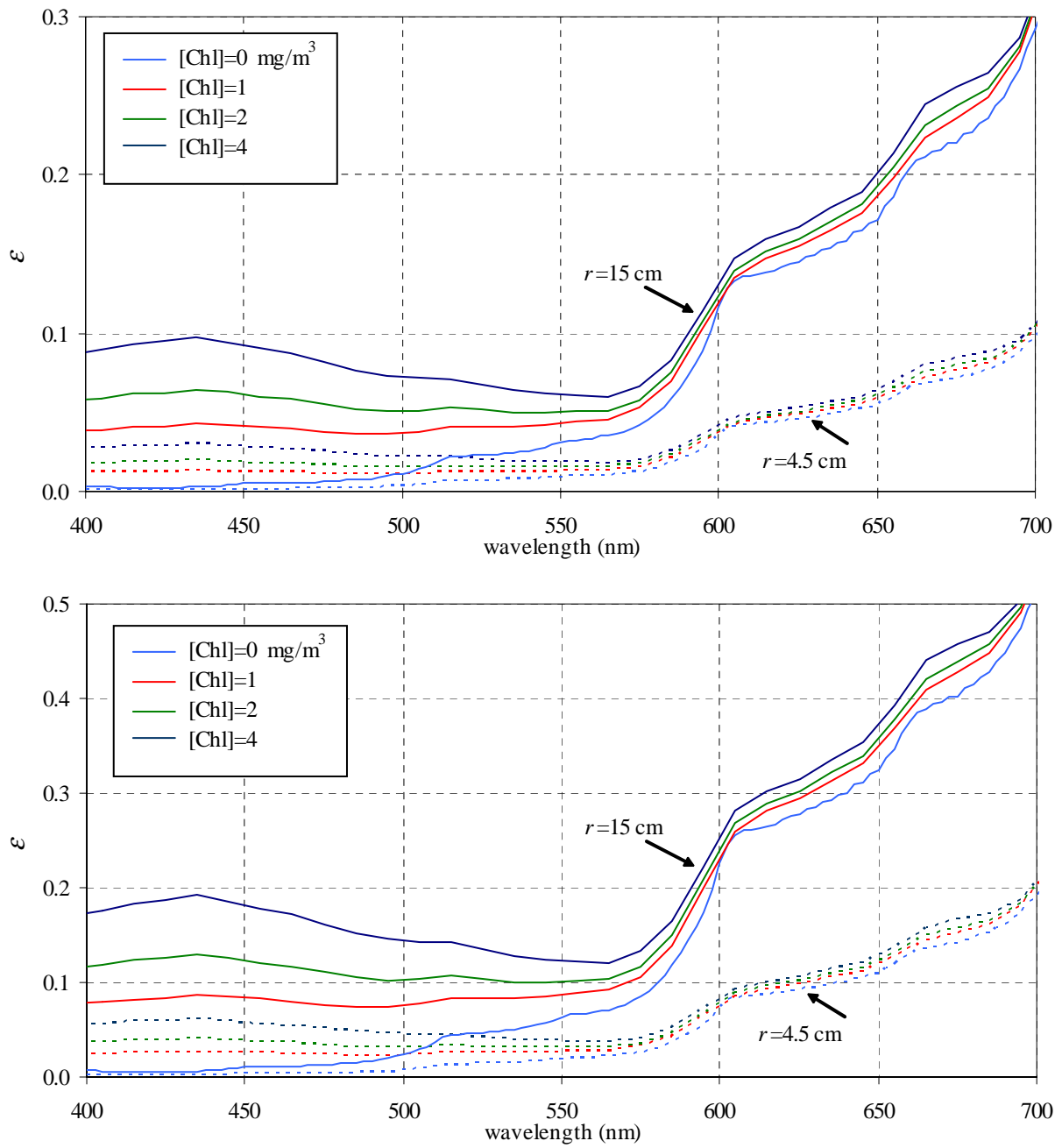


Fig. 4 — Percent shading error in case 1 waters as predicted by Eq. (1) for Sun angles of 20 deg (top) and 40 deg (bottom) and two disk radii: 0.045 m and 0.15 m

Table 3 — Nomenclature

a	beam absorption coefficient (1/m)
b	beam scattering coefficient (1/m)
b_b	backscattering coefficient (1/m)
E_d	downward irradiance (W/m^2)
ε	shading error
ε_s	shading error due to sensor head only
ε_b	shading error due to buoy only
ε_B	shading error of L_{uB}
ε_{sky}	shading error for skylight
ε_{Sun}	shading error for direct sunlight
ε_w	shading error of L_{uw}
f	fraction of total E_d that is due to diffuse skylight
I	vector of illumination-condition weighting factors
k	constant in Eq. (1)
K_{Lu}	diffuse attenuation coefficient for upwelling radiance
L_u	upwelling radiance ($\text{W}/\text{m}^2/\text{sr}$)
L_u^m	upwelling radiance measured by a sensor
L_u^t	upwelling radiance in the absence of shading
L_{uB}	portion of upwelling radiance due to signal reflected off seafloor
L_{uw}	portion of upwelling radiance due to in-water scattering
n_w	index of refraction of water relative to air, $n_w = 1.338$
r, r_s	sensor head radius
r_b	buoy radius (m)
r_{fov}	radius of radiance sensor field-of-view projected onto the seafloor
R_b	seafloor albedo
s	geometric pathlength (m)
W	ray-tracing result in the absence of shading
W_s	ray-tracing result in the presence of shading
w	photon weight
x, y, z	Cartesian coordinates
x_s	position of center of instrument shadow on seafloor
z_b	depth of bottom of buoy
z_{bot}	water depth (m)
z_0	depth of shadow along sensor's line-of-sight
z_s	sensor head depth
$\tilde{\beta}$	scattering phase function
θ_0	solar zenith angle (in air)
θ_{0w}	in-water solar zenith angle
λ	wavelength
μ_{0w}	cosine of in-water solar zenith angle
χ	$1 + 1/\mu_{0w}$
ω_0	single-scattering albedo, $\omega_0 = b/(a+b)$

2. ANALYTICAL APPROXIMATIONS

2.1 Sensor Self-shading in Deep Water

A model for the self-shading error of a cylindrical radiometer can be derived analytically by considering the idealized case illustrated in Fig. 5. An infinitesimally small sensor with infinitesimally small field of view (FOV) is positioned at the center of a sensor head. The sensor head is located at the sea surface and is modeled as a two-dimensional shading disk with radius r_s . The solar illumination is collimated, the water is optically deep, and the scattering by water is assumed to be negligibly small. The goal is to determine how much the measured upwelling radiance L_u^m is reduced by the shadow that falls across the sensor's line of sight (LOS). Although the derivation to follow is for a sensor placed at the sea surface, it is equally valid for a sensor placed at some depth below the surface.

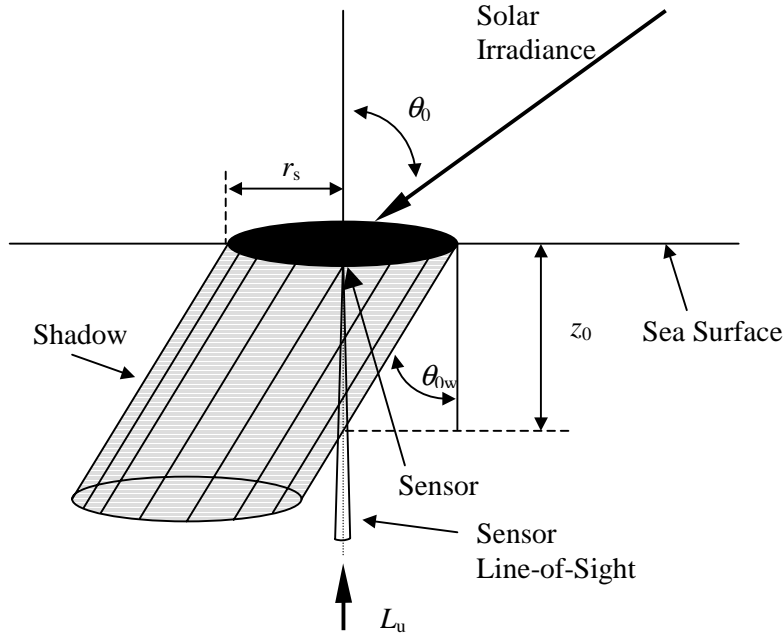


Fig. 5 — Self-shading of an upwelling radiometer as modeled by a horizontal two-dimensional disk

Following Gordon and Ding [8], we observe that the depth above which the sensor's LOS is within the disk's shadow is

$$z_0 = \frac{r_s}{\tan \theta_{0w}}. \quad (3)$$

The in-water solar zenith angle θ_{0w} is related to the above-water solar zenith angle by Snell's law [19],

$$\theta_{0w} = \sin^{-1} \left(\frac{\sin \theta_0}{n_w} \right), \quad (4)$$

where n_w is the relative index of refraction of seawater with respect to air ($n_w = 1.338$). Because no light is scattered into the detector from within the shaded region, the magnitude of upwelling radiance at the

sensor is that at depth z_0 (directly below the sensor) attenuated back up to the sensor. Because the sensor has a small FOV, the attenuation of this upwelling light from $z = z_0$ to $z = 0$ is quantified by the beam absorption coefficient a , and the radiance measured by the sensor at $z = 0$ is

$$L_u^m = L_u^t(z_0) \exp(-a z_0), \quad (5)$$

where $L_u^t(z)$ is the true upwelling radiance (i.e., that which would exist in the absence of any shading). The depth dependence of $L_u^t(z)$ can be approximated with

$$L_u^t(z) = L_u^t(0) \exp(-K_{Lu} z), \quad (6)$$

where K_{Lu} is a depth-averaged value of the diffuse attenuation coefficient for $L_u(z)$,

$$K_{Lu}(z) \equiv -\frac{d[\ln(L_u(z))]}{dz}. \quad (7)$$

(Note that for our specification of negligible scattering, $K_{Lu}(z)$ is essentially constant with depth.) From Eq. (6), the upwelling radiance at depth z_0 is

$$L_u^t(z_0) = L_u^t(0) \exp(-K_{Lu} z_0), \quad (8)$$

and the substitution of this expression into Eq. (5) gives

$$\begin{aligned} L_u^m &= L_u^t(0) \exp(-K_{Lu} z_0) \exp(-a z_0) \\ &= L_u^t(0) \exp[-(K_{Lu} + a) z_0]. \end{aligned} \quad (9)$$

Substituting Eq. (3) into Eq. (9) gives

$$L_u^m = L_u^t(0) \exp\left[\frac{-(K_{Lu} + a) r_s}{\tan \theta_{0w}}\right]. \quad (10)$$

Gordon and Ding [8] use the approximation $K_{Lu} = a$, which reduces Eq. (10) to

$$L_u^m = L_u^t(0) \exp\left(\frac{-2a r_s}{\tan \theta_{0w}}\right). \quad (11)$$

However, a better approximation to K_{Lu} is $K_{Lu} = a/\cos \theta_{0w}$, which when substituted into Eq. (10) gives

$$L_u^m = L_u^t(0) \exp\left[-a r_s \left(\frac{1}{\sin \theta_{0w}} + \frac{1}{\tan \theta_{0w}}\right)\right]. \quad (12)$$

The difference between Eqs. (11) and (12) is only significant for large values of θ_{0w} . From Eqs. (11) and (12), the fractional shading error is

$$\varepsilon = \left[1 - \frac{L_u^m}{L_u^t} \right] = \left[1 - \exp(-k a r) \right], \quad (13)$$

where $k = 2/\tan\theta_{0w}$ [from Eq. (11)] or $k = (1/\tan\theta_{0w} + 1/\sin\theta_{0w})$ [from Eq. (12)], depending on the approximation chosen for K_{Lu} . Note that Eq. (13) is the same as that provided earlier as Eq. (1). Table 4 shows values of k obtained three different ways: with $k = 2/\tan\theta_{0w}$, with $k = (1/\tan\theta_{0w} + 1/\sin\theta_{0w})$, and from the numerically obtained values shown in Table 1 for a point sensor. [Recall that values of θ_0 and θ_{0w} are related by Eq. (4).] The values obtained with $k = (1/\tan\theta_{0w} + 1/\sin\theta_{0w})$ agree with the numerical results far better than do those obtained with $k = 2/\tan\theta_{0w}$, especially at large solar zenith angles. This confirms that $K_{Lu} = a/\cos\theta_{0w}$ is a better approximation than $K_{Lu} = a$. This also means that the analytical approach presented by Gordon and Ding [8] would have more closely matched their numerical results had they used $K_{Lu} = a/\cos\theta_{0w}$.

Table 4 —Values of k for a Radiance Point Sensor Obtained Three Different Ways

θ_0 (deg)	$k = 2/\tan\theta_{0w}$	$k = (1/\tan\theta_{0w} + 1/\sin\theta_{0w})$	k computed from Table 1
10	15.28	15.35	16.58
20	7.56	7.69	8.43
30	4.96	5.16	5.54
40	3.65	3.91	4.18
50	2.86	3.18	3.39
60	2.36	2.72	2.84
70	2.03	2.44	2.48

In Eq. (13) the parameters a and r appear only as a product; an increase in a has the same effect on shading as an increase in r . The self-shading error predicted by Eq. (13) with $k = (1/\tan\theta_{0w} + 1/\sin\theta_{0w})$ is shown in Fig. 6 as a function of the product ($a r$) and in Fig. 7 vs Sun angle. As should be expected, the shading error depends strongly on the Sun's position. In the extremes (not shown in Fig. 6), the error is 100% for all ($a r$) when $\tan\theta_0 = 0$ deg and approaches zero for all ($a r$) as $\tan\theta_0$ approaches 90 deg. The shading error for general sky conditions can be computed with Eq. (2). The value of $k = 4.61$ computed by Gordon and Ding for diffuse skylight equals that for direct sunlight at approximately $\theta_0 = 35$ deg [Table 4], and, therefore, we can retain a purely analytical model for self-shading if we use $\theta_0 = 35$ deg to represent skylight. It can be seen in Fig. 6 that the shading error increases rapidly with increasing ($a r$) once the error is greater than about 10%. This indicates that, given an upper limit on the expected value of a , one should attempt to make the radiometer small enough and θ_0 large enough to keep the shading error under 10%. On the other hand, though, taking radiometer measurements at large values of θ_0 can lead to other difficulties, such as low signal-to-noise ratios and capillary wave interference. Because the absorption coefficient of water is high at red and infrared wavelengths, self-shading is likely to always place an upper wavelength limit on usable radiometer data.

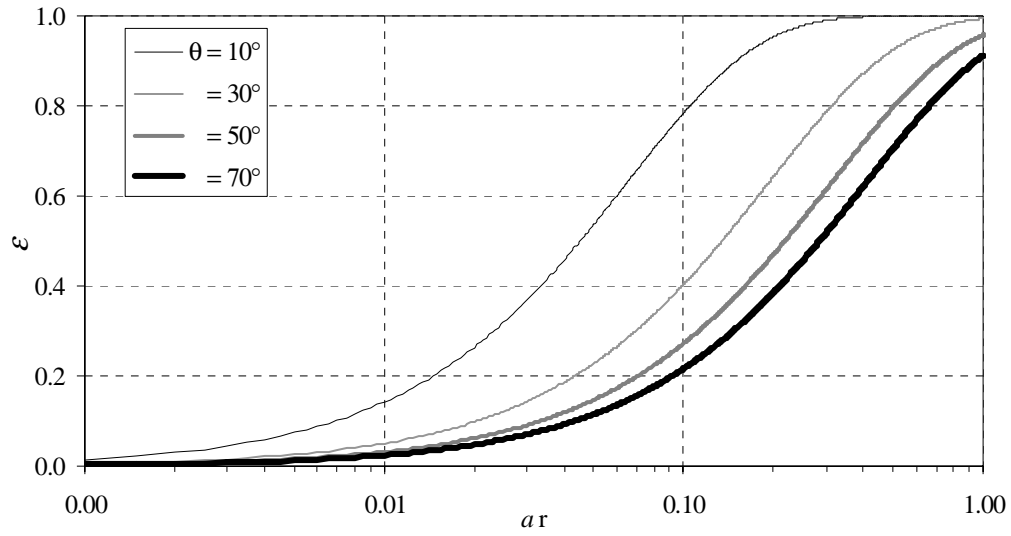


Fig. 6 — Self-shading error of a cylindrical instrument as predicted by Eq. (13) with $k = (1/\tan\theta_{0w} + 1/\sin\theta_{0w})$ for direct sunlight from the indicated solar zenith angles

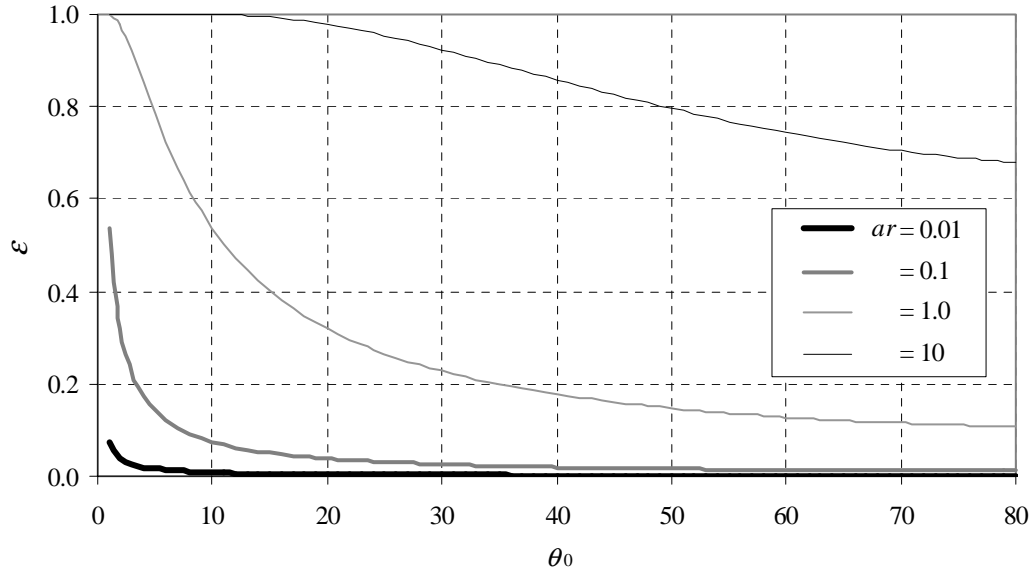


Fig. 7 — Self-shading error of a cylindrical instrument as predicted by Eq. (13) with $k = (1/\tan\theta_{0w} + 1/\sin\theta_{0w})$ for various values of (ar)

2.2 Buoy Shading in Deep Water

Figure 8 shows the idealized case of a two-dimensional circular buoy that is located at some distance above a submerged upwelling radiance sensor. We can use this to get an analytical approximation to the shading error generated by a buoy. We use all the same assumptions as in the previous section and as illustrated in Fig. 5 except that the sensor is moved a distance z_s below the shading disk and the radius of the shading disk is taken to be that of the buoy, r_b .

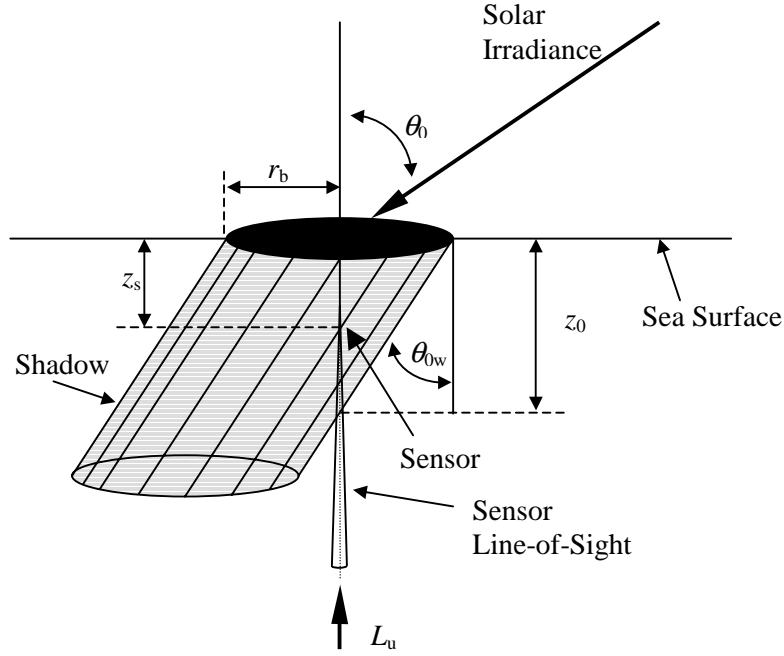


Fig. 8 — Shading of an upwelling radiance sensor by a buoy modeled as a horizontal disk with radius r_b

The depth to which the shadow lies across the sensor's LOS is

$$z_0 = \frac{r_b}{\tan \theta_{0w}}. \quad (14)$$

The radiance at the sensor is equal to that at depth z_0 attenuated back up to the sensor depth z_s ,

$$L_u^m = L_u^t(z_0) \exp[-a(z_0 - z_s)]. \quad (15)$$

The depth dependence of the true radiance (in the absence of shading) can be expressed as

$$L_u^t(z) = L_u^t(z_s) \exp[-K_{Lu}(z - z_s)]. \quad (16)$$

For the specific depth $z = z_0$,

$$L_u^t(z_0) = L_u^t(z_s) \exp[-K_{Lu}(z_0 - z_s)]. \quad (17)$$

Combining Eqs. (15) and (17), we obtain

$$L_u^m = L_u^t(z_s) \exp[-(K_{Lu} + a)(z_0 - z_s)]. \quad (18)$$

Substituting $K_{Lu} = a/\cos \theta_{0w}$ and Eq. (14) into Eq. (18),

$$L_u^m = L_u^t(z_s) \exp \left[- \left(\frac{1}{\tan \theta_{0w}} + \frac{1}{\sin \theta_{0w}} \right) a (r_b - z_s \tan \theta_{0w}) \right], \tan \theta_{0w} > \frac{r_b}{z_s},$$

which gives a shading error of

$$\varepsilon = \begin{cases} 1 - \exp \left[- \left(\frac{1}{\tan \theta_{0w}} + \frac{1}{\sin \theta_{0w}} \right) a (r_b - z_s \tan \theta_{0w}) \right], & \tan \theta_{0w} < \frac{r_b}{z_s} \\ 0, & \tan \theta_{0w} > \frac{r_b}{z_s} \end{cases}. \quad (19)$$

Note that Eq. (19) reduces to Eq. (13) if $z_s = 0$. The shading error due to a buoy depends on a and on r_b in a similar manner as for sensor-head self-shading [Eq. (13)]. As shown in Fig. 9, however, the dependence of ε on solar zenith angle is very different, specifically because the error is zero when $\tan \theta_{0w} > r_b/z_s$. Values for r_b and z_s in Fig. 9 include those representative of the Hyper-TSRB ($r_b = 0.15$ m and $z_s = 0.54$ m).

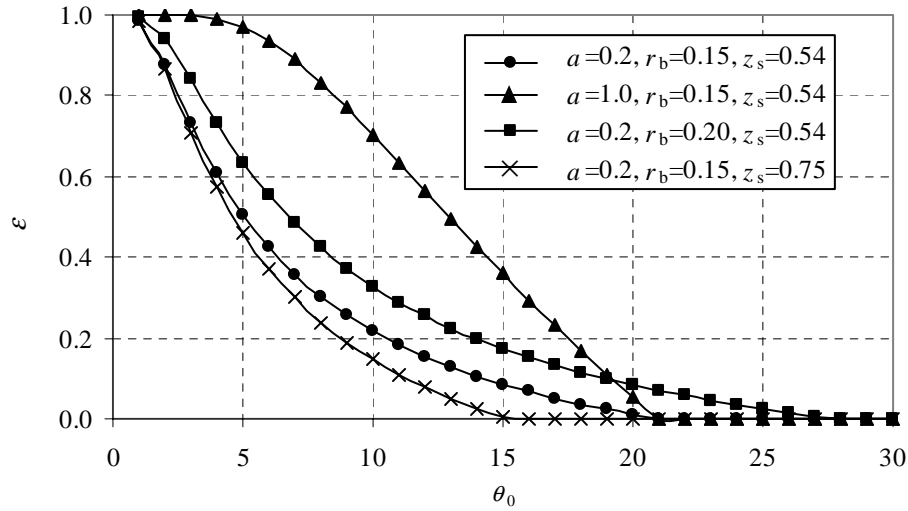


Fig. 9 — Shading error caused by a buoy as predicted by Eq. (19). Absorption coefficient (m^{-1}), buoy radius (m), and sensor depth (m) are as indicated.

2.3 Putting it Together: Self-shading of Buoyed Radiometers in Deep Water

For Satlantic's Hyper-TSRB, $r_b = 0.15$ m and $z_s = 0.54$ m. Therefore, from Eq. (19), the buoy is expected to shade the sensor if

$$\tan \theta_{0w} < 0.278,$$

or, equivalently,

$$\theta_{0w} < 16 \text{ deg}, \quad \theta_0 < 21 \text{ deg}.$$

Figure 10 shows the self-shading error due to the Hyper-TSRB buoy as predicted by Eq. (19) and the self-shading error due to the sensor head (with $r_s = 0.045$ m) as predicted by Eq. (13) with $k = (1/\tan\theta_{0w} + 1/\sin\theta_{0w})$. As expected, the shading due to the buoy dominates at small solar zenith angles, whereas only the sensor self-shading contributes at large solar zenith angles. Note that the buoy shading error goes to zero near $\theta_0 = 21$ deg, as predicted above.

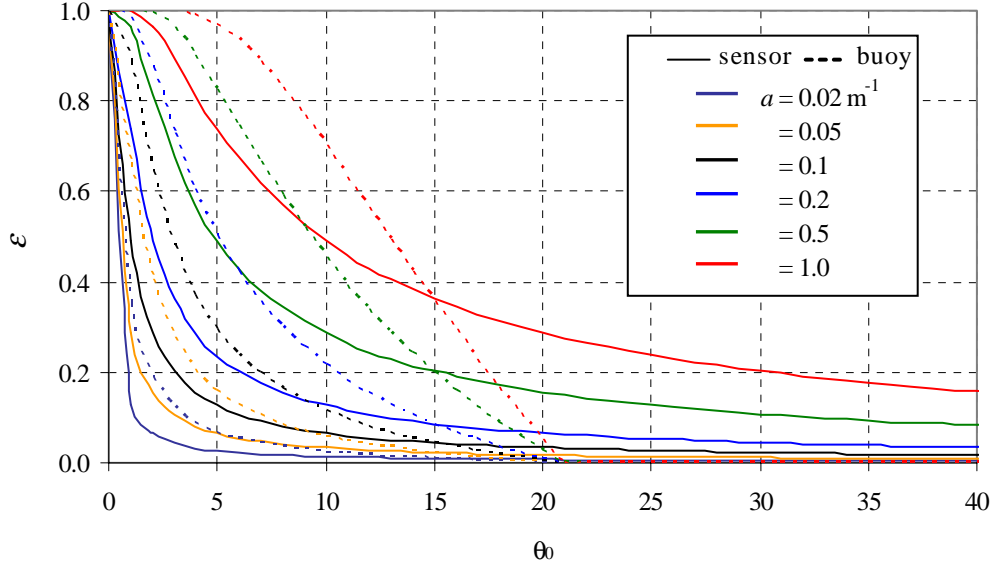


Fig. 10 — Self-shading error of the Hyper-TSRB sensor head and buoy in deepwater as predicted by Eqs. (13) (solid lines) and (19) (dashed lines), respectively, for various values of absorption coefficient a

Under the assumptions used to derive Eqs. (13) and (19), the shading due to the sensor and that due to the buoy are never additive. As illustrated in the center image of Fig. 11, the length of water column below the sensor that is shaded by the buoy is identical to that shaded by the sensor when the Sun angle is such that it matches the angle of a line connecting the outer edge of the buoy to the outer edge of the sensor, i.e., $\tan\theta_{0w} = (r_s - r_b)/(z_s - z_b)$. For the Hyper-TSRB, this occurs when $\theta_{0w} = 11$ deg ($\theta_0 = 15$ deg). As can be seen in Fig. 10, this is the Sun angle at which the shading error due to the buoy (in the absence of sensor shading) equals the shading error due to the sensor head (in the absence of a shading buoy). For smaller solar zenith angles, the depth of the shadow below the sensor due to the buoy is deeper than the depth of the shadow due to the sensor head (Fig. 11, right image), and the sensor head contributes no shading beyond that already caused by the buoy. Conversely, the presence of the buoy contributes no additional shading to that caused by the sensor head for larger solar zenith angles (Fig. 11, left image). Therefore, the total shading due to a buoyed radiometer is simply the larger of the two effects. Our complete analytical model for self-shading of buoyed radiometers in deepwater is

$$\mathcal{E} = \max(\mathcal{E}_s, \mathcal{E}_b), \quad (20)$$

where \mathcal{E}_s is the error predicted by Eq. (13) using the sensor head radius and \mathcal{E}_b is that predicted with Eq. (19) using the buoy radius. Equivalently, we can write Eq. (20) as

$$\varepsilon = \begin{cases} 1 - \exp\left[-\left(1/\tan\theta_{0w} + 1/\sin\theta_{0w}\right)a r_s\right], & \tan\theta_{0w} > \frac{(r_s - r_b)}{(z_s - z_b)} \\ 1 - \exp\left[-\left(1/\tan\theta_{0w} + 1/\sin\theta_{0w}\right)a (r_b - z_s \tan\theta_{0w})\right], & \tan\theta_{0w} < \frac{(r_s - r_b)}{(z_s - z_b)} \end{cases}. \quad (21)$$

The overall shading error of the Hyper-TSRB as predicted by Eq. (21) is shown in Fig. 12. This figure emphasizes the importance of avoiding Hyper-TSRB L_u measurements when θ_0 is small, especially if a is large.

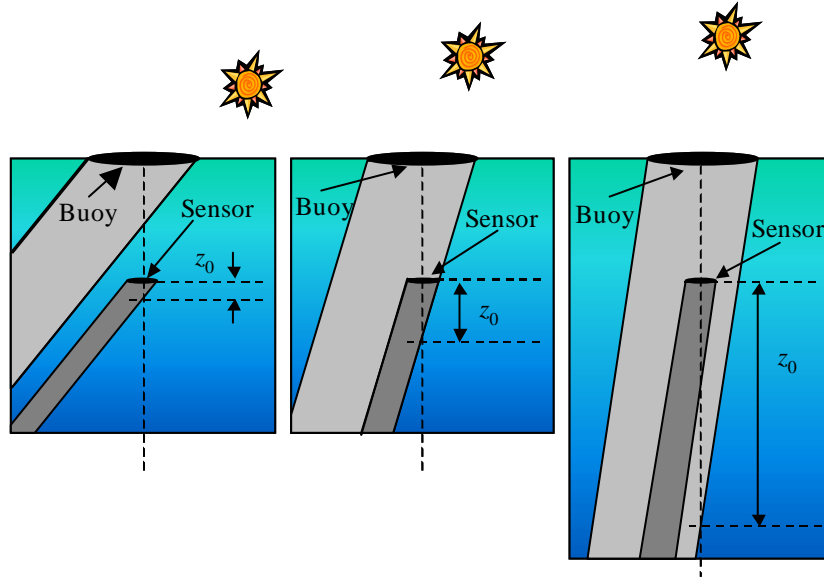


Fig. 11 — The value of z_0 for a buoyed radiometer is determined by the sensor for large solar zenith angles (left) and by the buoy for small solar zenith angles (right). The special Sun position for which the sensor and buoy give the same value of z_0 (center) occurs when $\tan\theta_{0w} = (r_s - r_b)/(z_s - z_b)$.

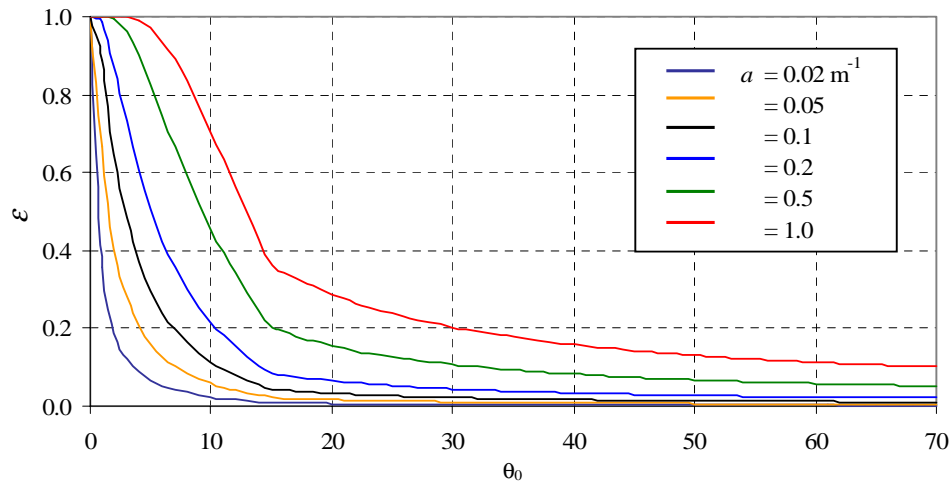


Fig. 12 — Self-shading of the Hyper-TSRB (as predicted by Eq. (21)) for various values of absorption coefficient a . Higher values of a correspond to higher values of ε .

2.4 Self-shading in Shallow Water: Infinitesimal FOV

Under the assumptions we have been using of infinitesimal sensor FOV and very low water scattering, the presence of the seafloor affects the amount of self-shading if and only if the depth of the shading below the sensor is greater than the distance between the sensor and the seafloor. As illustrated in Fig. 13 for the case of cylindrical radiometer placed at the sea surface, if $z_0 > z_{\text{bot}}$, then the entire water column (and seafloor) within the sensor's LOS is in shadow and the shading error is 100%. We conclude from this that we should expect the amount of self-shading of a cylindrical instrument to be important whenever the in-water Sun angle is small enough to satisfy

$$\theta_{0w} < \tan^{-1} \left[\frac{r_s}{z_{\text{bot}} - z_s} \right], \quad (22)$$

where r_s is the radius of the sensor head, z_{bot} is the depth of the seafloor, and z_s is the depth of the sensor ($z_s = 0$ in Fig. 13). Likewise, we can expect 100% shading from the float on a buoyed radiometer whenever

$$\theta_{0w} < \tan^{-1} \left[\frac{r_b}{z_{\text{bot}} - z_b} \right], \quad (23)$$

where r_b and z_b are the radius and depth of the buoy. Figure 14 shows the maximum Sun angles (in air) that satisfy Eq. (22) for the Hyper-TSRB sensor-head radius and Eq. (23) for the Hyper-TSRB buoy radius. The angle increases dramatically as the instrument nears the seafloor.

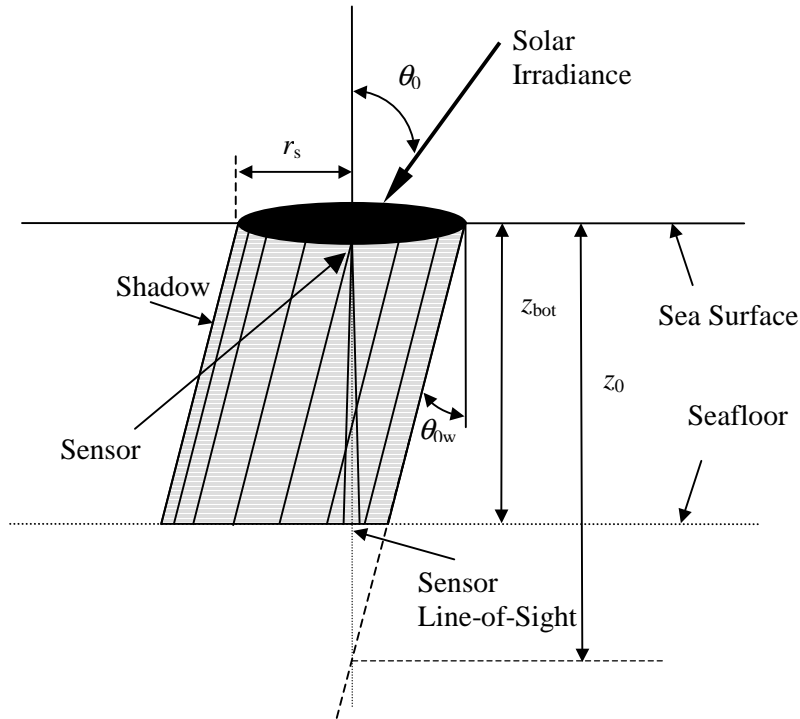


Fig. 13 — Self-shading in shallow water of a radiometer with infinitesimal FOV

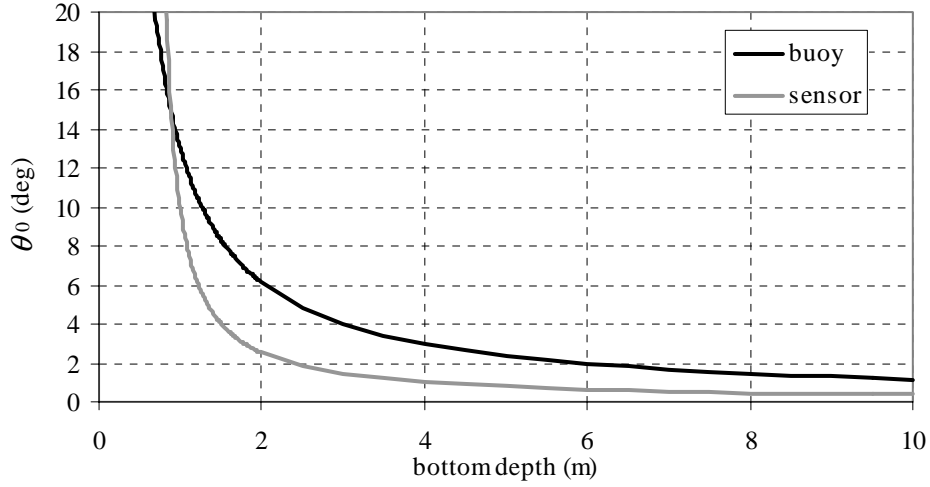


Fig. 14 — Solar zenith angle below which the shadow on the seafloor lies directly below sensor

We can combine Eqs. (21) through (23) to obtain a model for self-shading in shallow waters:

$$\varepsilon = \begin{cases} 1 & \theta_{0w} < \theta_{0wc} \\ 1 - \exp\left[-(1/\tan\theta_{0w} + 1/\sin\theta_{0w})a r_s\right], & \tan\theta_{0w} > (z_s - z_b)/(r_s - r_b) \\ 1 - \exp\left[-(1/\tan\theta_{0w} + 1/\sin\theta_{0w})a(r_b - z_s \tan\theta_{0w})\right], & \tan\theta_{0w} < (z_s - z_b)/(r_s - r_b) \end{cases}, \quad (24)$$

where

$$\theta_{0wc} = \min\left\{\tan^{-1}\left[\frac{r_s}{z_{bot} - z_s}\right], \tan^{-1}\left[\frac{r_b}{z_{bot} - z_b}\right]\right\}. \quad (25)$$

2.5 Self-shading in Shallow Water: Finite FOV

The shading model of Eq. (24) was derived for a sensor with very narrow FOV, and it is unlikely to perform satisfactorily in shallow water for a sensor with a FOV of more than a few degrees (such as the 8.5 deg half-angle FOV for the Hyper-TSRB). Therefore, we derive here a more complex model by combining an estimate of the amount of shadowing of the seafloor component of the measured upwelling radiance (for a sensor with finite FOV) with an estimate of the shading of the water component of the measured upwelling radiance. We define the seafloor (or bottom) component of the measured upwelling radiance as the portion of the photons detected by the sensor that have reflected off the seafloor at some point in their paths. The water column component of the measured upwelling radiance is then defined as all remaining detected photons (i.e., those that have never interacted with the seafloor). Note that the water column component of the total measured radiance is negligible if the instrument is very close to the bottom. We can use a modified version of Eq. (21) to give us a good estimate of the shading error of the water column component of the measured upwelling radiance, but we have to derive a new model for the shading of the seafloor component of the measured upwelling radiance.

2.5.1 Shading of the Seafloor

If the seafloor is horizontal and water scattering is negligible, then both the sensor FOV and the shading disk project circles on the seafloor. For a Lambertian seafloor and a sensor that responds equally

to light from all directions within its FOV, the percent shading due to the shadow on the seafloor approximately equals the percent of the FOV circle that is overlapped by the shading circle. The task then is to determine the size and locations of the two circles on the seafloor and to compute the amount of overlap. Consider a radiometer at depth z_s centered at horizontal position $x = 0$ and a shading disk of radius r_d positioned at $x = 0$ and depth z_d (see Fig. 15). (For the case of self-shading of a sensor head, $r_d = r_s$ and $z_d = z_s$, whereas for the case of shading by a buoy, $r_d = r_b$ and $z_d = z_b$.) Define the x-axis (in the horizontal plane) such that the positive-x direction is looking away from the Sun. The resulting shadow on the seafloor is of radius r_s and is centered at $x_d = (\tan \theta_{\theta_w})(z_{\text{bot}} - z_d)$, where z_{bot} is the total water depth. The FOV on the seafloor is centered at $x = 0$ and has radius $r_{\text{fov}} = (\tan \theta_{\text{fov}})(z_{\text{bot}} - z_s)$, where θ_{fov} is the FOV half-angle. The equations for the two circles are

$$(x - x_d)^2 + y^2 = r_d^2,$$

$$x^2 + y^2 = r_{\text{fov}}^2.$$

The two circles are both centered on the x-axis (i.e. $y = 0$). As illustrated in Fig. 16, one of four situations exists:

- a) The two circles do not overlap (as illustrated in Fig. 15). This is most likely when the solar zenith angle is large. This condition is satisfied when the leftmost extent of the shade circle lies to the right of the rightmost extent of the FOV circle, $(x_d - r_d) > r_{\text{fov}}$. The shading error (of the seafloor component of L_u) is zero.
- b) The FOV circle is completely inside the shade circle. This can happen at small solar zenith angles and very shallow water. The condition for this is that the leftmost extent of the FOV circle lies to the right of the leftmost extent of the shade circle, $(-r_{\text{fov}}) > (x_d - r_d)$. The shading error is 1 (100%).
- c) The shade circle is completely inside the FOV circle. This can happen at small solar zenith angles and moderate water depth. The condition for this is that the rightmost extent of the shade circle is to the left of the FOV circle, $(x_d + r_d) < r_{\text{fov}}$. The shading error is the area of the shade circle divided by that of the FOV circle.
- d) The two circles partially overlap. This is the case if none of the other three conditions are met. If the circles intersect, they only intersect at one value of $x = x_{\text{int}}$ (\pm some value of y). The overlap is the area under the shade circle from the left-hand side of the shade circle ($x = x_d - r_d$) to $x = x_{\text{int}}$ plus the area under the FOV curve from $x = x_{\text{int}}$ to $x = r_{\text{fov}}$. The shading error is this area divided by the total FOV area, πr_{fov}^2 .

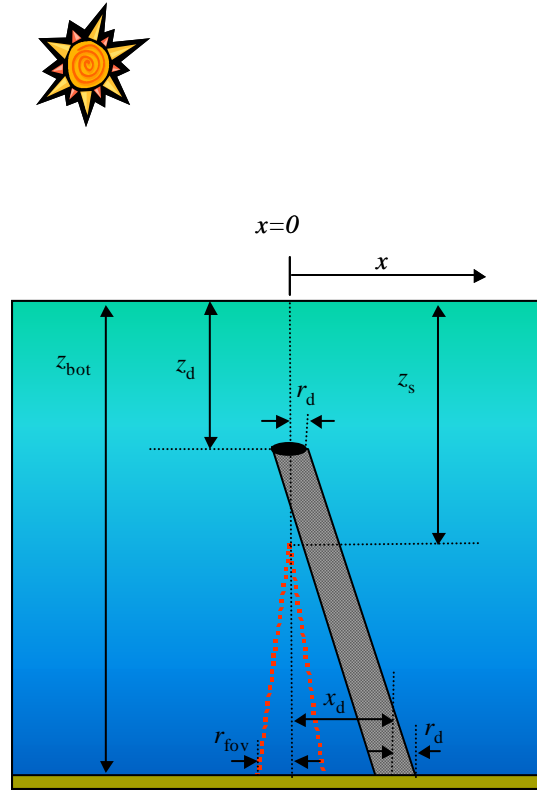


Fig. 15 — Configuration for investigation of potential overlap of shadow and FOV. This image specifically shows the circumstance in which there is no overlap of FOV and shadow on the seafloor.

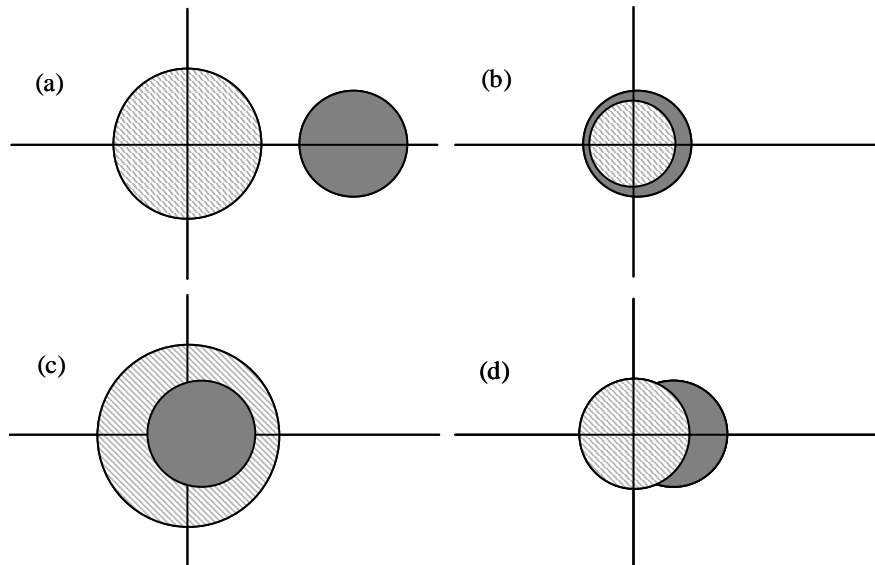


Fig. 16 — Four possibilities of shadow (gray) overlap with FOV on seafloor (striped): (a) no overlap; (b) FOV entirely covered by shadow; (c) entire shadow lies within FOV; (d) the two circles overlap

Summarizing mathematically,

$$\mathcal{E} = \left\{ \begin{array}{ll} 0, & (x_d - r_d) > r_{fov}, \\ 1, & (-r_{fov}) > (x_d - r_d), \\ (r_d / r_{fov})^2, & (x_d + r_d) < r_{fov}, \\ \frac{2}{\pi r_{fov}^2} \left(\int_{x_d - r_d}^{x_{int}} \sqrt{r_d^2 - (x - x_d)^2} dx + \int_{x_{int}}^{r_{fov}} \sqrt{r_{fov}^2 - x^2} dx \right), & (-r_{fov}) < (x_d - r_d) < r_{fov} \text{ and } r_{fov} < (x_d + r_d), \end{array} \right\}, \quad (26)$$

where

$$x_d = \tan \theta_{0w} (z_{bot} - z_d), \quad r_{fov} = [\tan \theta_{fov} (z_{bot} - z_s)], \quad \text{and} \quad x_{int} = \frac{r_{fov}^2 - r_d^2 + x_d^2}{2x_d}.$$

Evaluation of the above integrals yields

$$\begin{aligned} \int_{x_d - r_d}^{x_{int}} \sqrt{r_d^2 - (x - x_d)^2} dx &= \left[\frac{x - x_d}{2} \sqrt{r_d^2 - (x - x_d)^2} + \frac{r_d^2}{2} \sin^{-1} \left(\frac{x - x_d}{r_d} \right) \right]_{x_d - r_d}^{x_{int}} \\ &= \frac{x_{int} - x_d}{2} \sqrt{r_d^2 - (x_{int} - x_d)^2} + \frac{r_d^2}{2} \sin^{-1} \left(\frac{x_{int} - x_d}{r_d} \right) + \pi r_d^2, \end{aligned}$$

and

$$\begin{aligned} \int_{x_{int}}^{r_{fov}} \sqrt{r_{fov}^2 - x^2} dx &= \left[\frac{x}{2} \sqrt{r_{fov}^2 - x^2} + \frac{r_{fov}^2}{2} \sin^{-1} \left(\frac{x}{r_{fov}} \right) \right]_{x_{int}}^{r_{fov}} \\ &= -\frac{x_{int}}{2} \sqrt{r_{fov}^2 - x_{int}^2} - \frac{r_{fov}^2}{2} \sin^{-1} \left(\frac{x_{int}}{r_{fov}} \right) + \frac{\pi r_{fov}^2}{4}, \end{aligned}$$

Results from Eq. (26) are shown in Fig. 17 for the Hyper-TSRB sensor head ($r_d = r_s$ and $z_d = z_s$) and Hyper-TSRB buoy ($r_d = r_b$ and $z_d = z_b$). It can be seen that shading by the buoy dominates at small solar zenith angles and large water depths, while shading from the sensor head dominates in very shallow water and large solar zenith angles. Unlike the deepwater case, it is possible for the shading contributions from the buoy and sensor head to be additive. Although it would be possible to account for this, we expect this effect to be minimal and will (analogous to Eq. (20)) take the overall shading error of the seafloor component of L_u to be

$$\mathcal{E} = \max(\mathcal{E}_s, \mathcal{E}_b), \quad (27)$$

where \mathcal{E}_s is obtained with Eq. (26) with $r_d = r_s$ and $z_d = z_s$ and \mathcal{E}_b is obtained with Eq. (26) with $r_d = r_b$ and $z_d = z_b$.

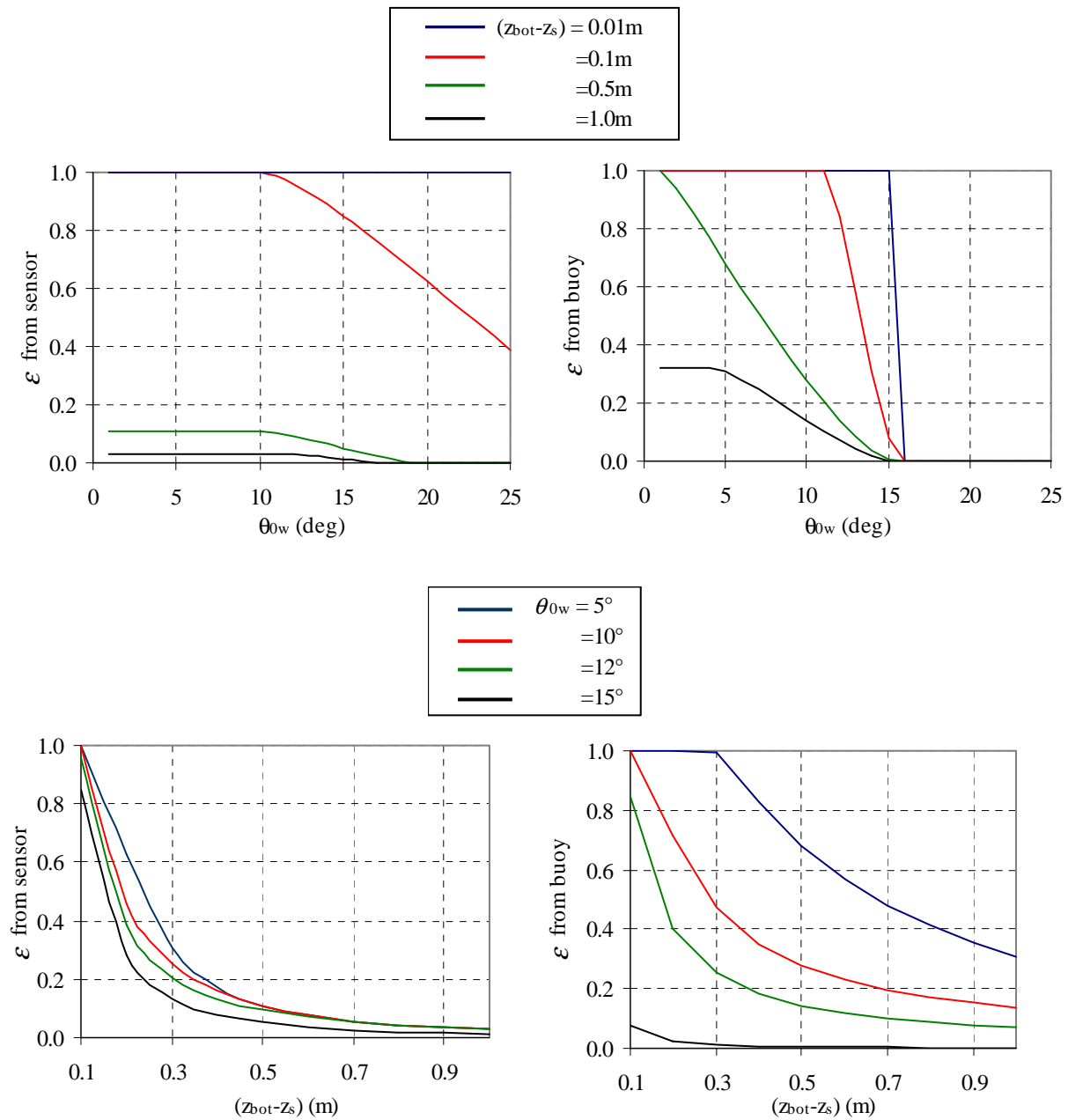


Fig. 17 — Percent shading due to sensor head shadow (left) and buoy shadow (right) on the seafloor. These curves are for a buoy with radius = 0.152 m located 0.54 m above a sensor with radius 0.05 m and FOV = 15 deg, for various Sun angles and heights of the sensor from the seafloor.

2.5.2 Combining Seafloor and Water Column Components

Now that we have developed a shading model for a buoyed radiometer far from the seafloor (Eq. (21)) and a shading model for a buoyed radiometer very close to the bottom (Eq. (27)), the next step is to determine the transition from one to the other. We choose to use a weighted sum of the two models based on the relative importance of the signal from the seafloor and the signal from the water column,

$$\mathcal{E} = \left(\frac{L_{uw}}{L_{uB} + L_{uw}} \right) \mathcal{E}_w + \left(\frac{L_{uB}}{L_{uB} + L_{uw}} \right) \mathcal{E}_B, \quad (28)$$

where \mathcal{E}_w is the error predicted by Eq. (21), \mathcal{E}_B is the error predicted by Eq. (27), L_{uw} is the portion of $L_u(z_s)$ that originates in the water column, and L_{uB} is the portion of $L_u(z_s)$ that originates at the seafloor. Equation (28) provides a continuous transition from one model to the other. The task at hand is to now estimate the values of L_{uw} and L_{uB} .

Continuing to assume a nearly collimated light field, the downward irradiance at the seafloor is related to that at the sensor by

$$E_d(z_{bot}) = E_d(z_s) \exp[-a(z_{bot} - z_s)/\mu_{0w}],$$

where $\mu_{0w} = \cos \theta_{0w}$. Assuming a Lambertian seafloor with a bottom albedo R_b , the upwelling radiance at the seafloor is

$$L_u(z_{bot}) = \frac{R_b E_d(z_s)}{\pi} \exp\left(-\frac{a(z_{bot} - z_s)}{\mu_{0w}}\right).$$

Attenuating this upwelling radiance from the seafloor to the sensor gives

$$\begin{aligned} L_{uB} &= \frac{R_b E_d(z_s)}{\pi} \exp\left(-\frac{a(z_{bot} - z_s)}{\mu_{0w}}\right) \exp[-a(z_{bot} - z_s)] \\ &= \frac{R_b E_d(z_s)}{\pi} \exp\left[-a\left(1 + \frac{z_{bot}}{\mu_{0w}}\right)(z_{bot} - z_s)\right]. \end{aligned}$$

On the other hand, the upwelling radiance that originates within the water column below the sensor can be approximated as the integral over the water column below the sensor of backscattered light times its attenuation back to the sensor,

$$L_{uw} = \int_{z_s}^{z_{bot}} \frac{b_b E_d(z')}{\pi \mu_{0w}} \exp[-a(z' - z_s)] dz',$$

where b_b is the backscattering coefficient (in m^{-1}) and $b_b/(\pi \mu_{0w})$ represents the probability per vertical meter traveled that a photon will be scattered into an infinitesimally small solid angle about the vertically upward direction divided by the size of that solid angle (in $m^{-1} sr^{-1}$). The value of b_b is related to the beam scattering coefficient b by $b_b \approx 0.02 b$ in turbid waters and $b_b \approx 0.04 b$ in clear ocean waters [19]. Substituting for $E_d(z')$, we obtain

$$\begin{aligned}
L_{uw} &= \int_{z_s}^{z_{bot}} \frac{b_b E_d(z_s)}{\pi \mu_{0w}} \exp(-a(z' - z_s)/\mu_{0w}) \exp[-a(z' - z_s)] dz' \\
&= \frac{b_b E_d(z_s)}{\pi \mu_{0w}} \int_{z_s}^{z_{bot}} \exp[-a(1 + 1/\mu_{0w})(z' - z_s)] dz' \\
&= \frac{b_b E_d(z_s)}{a \pi \mu_{0w} (1 + 1/\mu_{0w})} \{1 - \exp[-a(1 + 1/\mu_{0w})(z_{bot} - z_s)]\},
\end{aligned}$$

The relative contribution to $L_u(z_s)$ from the water column is

$$\begin{aligned}
\frac{L_{uw}}{L_{uB} + L_{uw}} &= \frac{b_b \{1 - \exp[-a \chi z_d]\}}{R_b a \mu_{0w} \chi \exp[-a \chi z_d] + b_b \{1 - \exp[-a \chi z_d]\}} \\
&= \frac{b_b \{1 - \exp[-a \chi z_d]\}}{b_b + (R_b a \mu_{0w} \chi - b_b) \exp[-a \chi z_d]},
\end{aligned} \tag{29}$$

where

$$z_d \equiv z_{bot} - z_s \text{ and } \chi \equiv \left(1 + \frac{1}{\mu_{0w}}\right).$$

The relative contribution to $L_u(z_s)$ from the seafloor is

$$\frac{L_{uB}}{L_{uB} + L_{uw}} = 1 - \frac{L_{uw}}{L_{uB} + L_{uw}}. \tag{30}$$

Figure 18 shows the fraction of the seafloor component to the overall upwelling radiance at the sensor as predicted by Eqs. (29) and (30). As should be expected, the influence of the bottom drops off very quickly with increasing depth away from the bottom if the bottom albedo is small or the water absorption coefficient is large. Figure 19 compares values of L_{uB}/L_u computed with Eqs. (29) and (30) to those computed from numerical simulations performed with Hydrolight (Sequoia Scientific, Inc.). The simulated values of L_{uB}/L_u were determined by running Hydrolight for a set of conditions and then running it a second time with the value of R_b doubled but all other parameters held the same. The difference in L_u between the two runs was assumed to be entirely due to the doubling of the bottom component. Although the agreement between the analytical and numerical results is not as good as we had hoped, Eq. (29) should be accurate enough for the purpose of melding together the bottom-component and water-component shading models. Nonetheless, future research in this area should include an attempt to improve upon Eq. (29).

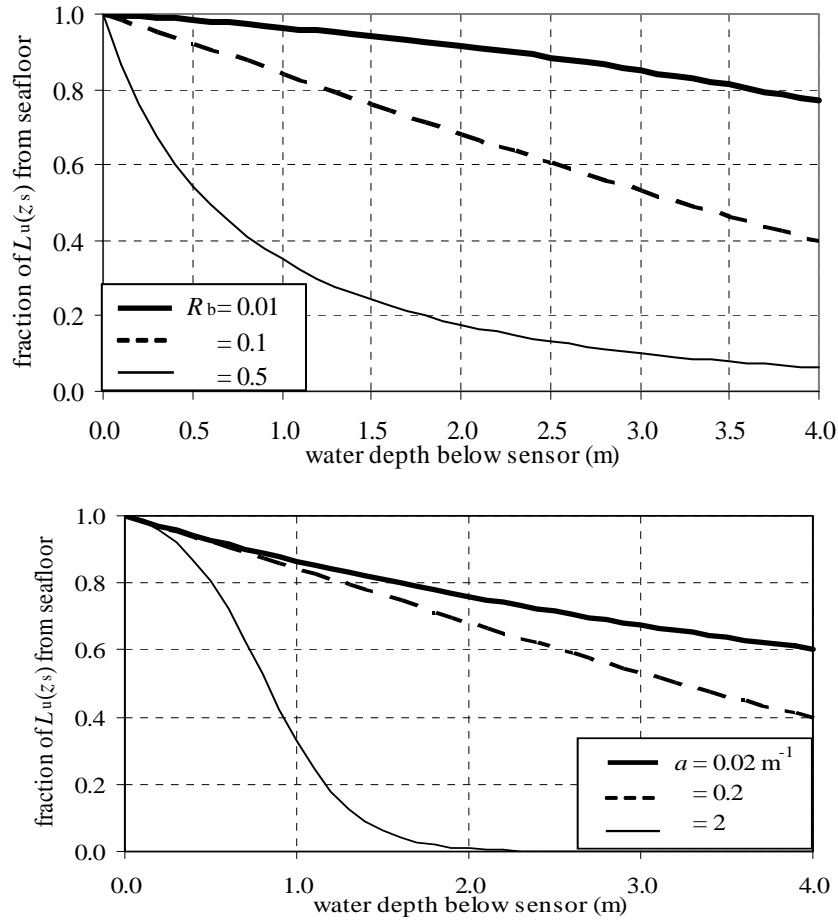


Fig. 18 — Fraction of measured upwelling radiance due to reflection off the seafloor. The top plot is for the case $a = 0.1 \text{ m}^{-1}$ and various values of R_b ; the bottom plot is for the case $R_b = 0.2$ and various values of c . In both cases, $b_b = 0.015 \text{ m}^{-1}$ and $\theta_0 = 10^\circ$.

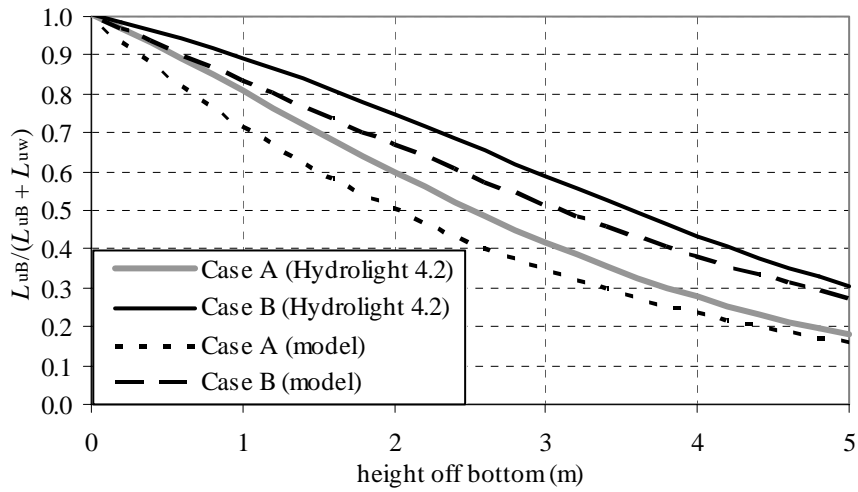


Fig. 19 — Comparison of numerically derived values of L_{uB}/L_u from Hydrolight 4.2 with values predicted with Eq. (29). Case A is for $a = 0.2 \text{ m}^{-1}$, $b = 0.8 \text{ m}^{-1}$, $b_b = 0.01466 \text{ m}^{-1}$, $R_b = 0.05$, and Sun in a black sky with $\theta_0 = 30^\circ$; Case B is for $a = 0.4$, $b = 0.4$, $b_b = 0.00733$, $R_b = 0.2$, and $\theta_0 = 50^\circ$.

2.5.3 The Complete Analytical Model

Combining the components we have so far derived, we have an algorithm for estimating the shading error of a buoyed radiometer as follows:

- Compute the shading of the water-column component of L_u with Eq. (21) and call this ε_w . Check that $(z_{\text{bot}} - z_s) > r_s / \tan \theta_{0w}$; if not, set ε_w to 1.
- Compute the shading of the seafloor signal due to the sensor head shadow with Eq. (27) and call this ε_B .
- Compute $L_{uw} / (L_{uB} + L_{uw})$ with Eq. (29).
- Compute the overall shading error for light with a specific incident direction with Eq. (28).
- Compute or estimate the angular dependence of the incident illumination. This may be computed with Hydrolight, for example, or estimated with a combination of direct sunlight and diffuse skylight (Eq. (2)).

Example values of f for use in Eq. (2) are provided in Fig. 20 and Table 5. These values, as computed with Hydrolight, are wavelength dependent for sunny conditions but wavelength independent when the percent cloudiness exceeds 25%. Example values of f are also provided in Ref. 22.

- Use the illumination conditions to obtain weights for the individual directional illumination bins. Sum the shading errors for each weighted bin to obtain the overall shading.

We implemented this algorithm in Matlab (The MathWorks, Inc., Natick, Massachusetts); however, this could easily be done in any standard programming language.

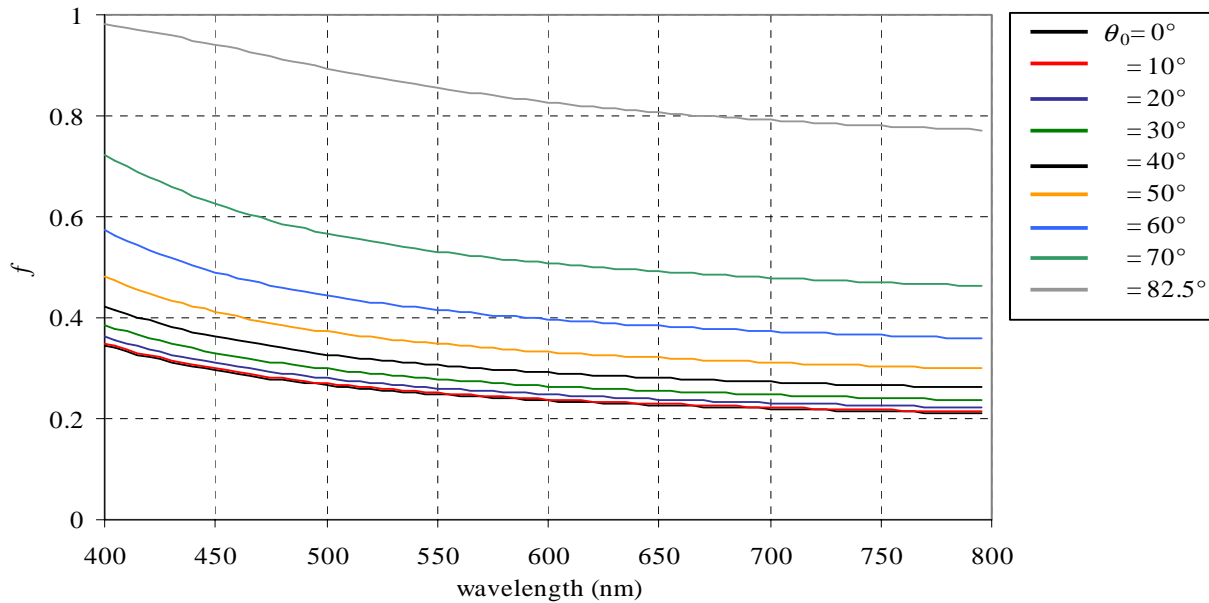


Fig. 20 — Modeled fraction f of the total downwelling irradiance that is diffuse skylight as a function of wavelength. These values are valid for clear conditions (less than 25% cloud cover). The value of f increases with increasing values of θ_0 .

Table 5 — Wavelength Independent Modeled Fraction of the Total Downwelling Irradiance that is Diffuse Skylight for Cloudy Conditions (Greater than 25% Cloud Cover)

percent cloudiness	f
26	0.347316
30	0.363000
50	0.475000
70	0.643009
90	0.867005

3. MONTE CARLO SIMULATIONS

3.1 The Modified BMC3D Code

In Monte Carlo simulations, the paths of individual photons are traced one at a time as they are scattered or reflected by their environment until they are either absorbed (e.g., by seawater or the seafloor) or scattered far away from the region of interest. The statistics of the paths of thousands or millions of simulated photons are used to quantify the in-water light field. In forward Monte Carlo simulations of the atmosphere-ocean system, photons are initiated from the Sun and traced through the atmosphere into the water column [19, 23]. However, very few of the simulated photons incident on the sea surface would be collected by a simulated instrument at a particular location in three-dimensional space. Therefore, in this research we use backward Monte Carlo simulations, in which photons are traced backward from the detector into the water column and followed until they are either absorbed or returned to the air side of the sea surface (Fig. 21) [19, 24]. Each photon that crosses the sea surface is assigned a weight that depends on the illumination conditions and on the direction of photon travel when it crosses the sea surface. The sum of all the photon weights gives the desired physical quantity.

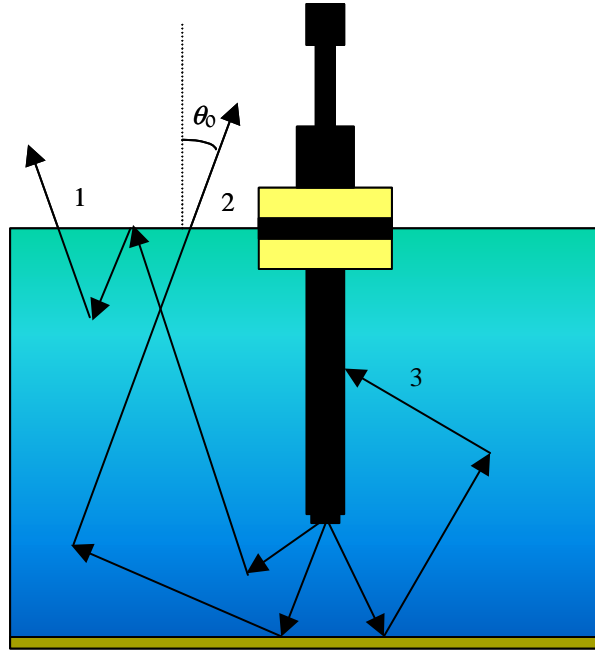


Fig. 21 — Backward ray tracing for a buoyed radiometer. Photon path 1 represents a photon that is backscattered by the water column into the detector, path 2 represents a photon that is reflected off the seafloor into the detector, and path 3 indicates a shaded photon path.

As part of the CoBOP program [3], Mobley and Sundman [25] developed the general oceanographic backward Monte Carlo computer code BMC3D to compute the upwelling radiance at a specified depth for a given set of water properties, depth, bottom albedo, and illumination conditions. Photons are emitted from the sensor depth in a manner consistent with the characteristics of the particular sensor being simulated and are traced until they cross the air-sea interface. The weight of each photon is reduced each time it scatters in the water, reflects off the seafloor, or internally reflects at the sea surface. A photon is discarded if its weight falls below a certain specified value. If the photon crosses the air-sea interface at any time, its weight is added to a tally. A semispherical grid is established at the start of the program that divides into bins the possible directions a photon could be traveling when it crosses the air-sea interface. This grid is defined based on a list of azimuthal and polar angles supplied by the user. When a photon crosses the air-sea interface, its weight is applied only to the bin corresponding to the direction the photon is traveling. In BMC3D the weighted sum for each bin is stored in an element of variable array W (named *wsum* in the code). Once all the photons have been traced, W contains the fraction of power emitted from the sensor that exits the sea surface within each directional bin. Independent of the ray tracing, another variable I (named *radsky* in the code) with the same dimensions as W is computed that provides the appropriate weighting for each directional bin for the particular illumination conditions being simulated. The total sensor response that BMC3D returns is the dot product of W and I , e.g.,

$$L_u = W \cdot I = \sum_i W_i I_i . \quad (31)$$

The illumination conditions, as represented by I , are computed using one of several atmospheric models available in BMC3D. The most sophisticated of these is based on the clear-sky irradiance model and associated routines developed by Gregg and Carder [26]. The Gregg and Carder clear-sky irradiances are adjusted by the model of Kasten and Czeplak [27] if the cloud fraction is greater than 25%.

Alternatively, the user can directly enter the Sun angle, the percent cloud cover, and the total solar irradiance at the sea surface. The routine then computes the normalized sky radiance by the semi-empirical model of Harrison and Coombes [28]. Note that, analogous to Eq. (2), the vector I can be approximated with

$$I_i = \begin{cases} 1-f, & \theta_0 \in \theta_i \\ \frac{f}{(n_i-1)}, & \theta_0 \notin \theta_i \end{cases},$$

where n_i is the length of vectors I and W .

Although the variables W and I are not accessible to the user in BMC3D, it is easy to modify the code to write the variables to an output file. It is then possible to separately store ray tracing results (which are independent of illumination conditions) and I values (which are independent of water optical properties, seafloor properties, and instrument type) and then later apply any illumination condition to any ray-tracing result using Eq. (31).

Several sensor types are included in BMC3D, including the Hyper-TSRB L_u sensor. The corresponding cumulative distribution function (cdf) used in BMC3D to initiate photon directions for the Hyper-TSRB is shown in Fig. 22.

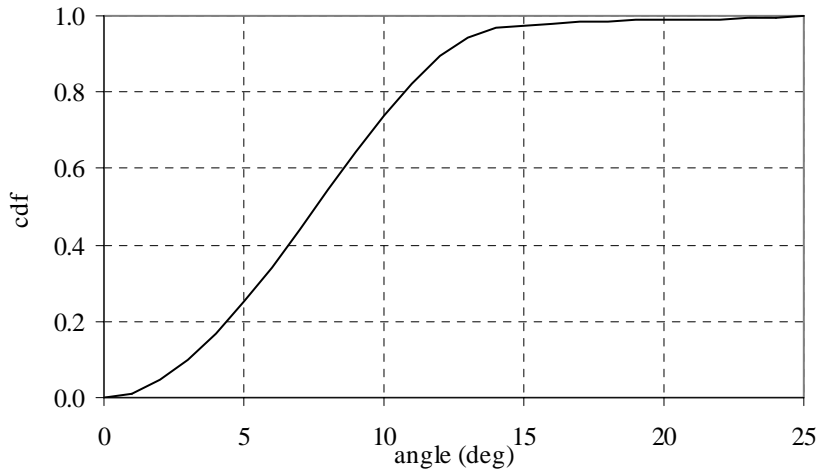


Fig. 22 — Cumulative distribution function for the Hyper-TSRB upwelling radiometer (derived from data provided by Satlantic)

For the investigation of self-shading, we modified BMC3D to compute radiometric quantities with and without the presence of a shading body and buoy, modeled as two concentric solid cylinders. For each set of environmental parameters, the difference between the sensor responses with and without shading is taken to be the amount of shading. To introduce shading, we added logical checks during each photon path to see whether or not the line segment defined by the photon path would intersect the three-dimensional cylinder(s) defining the instrument. If so, the photon was removed (i.e., the shading body was assumed to be perfectly absorbing).

The parametric equation for the line segment describing a photon path is

$$\begin{bmatrix} x \\ y \\ z \end{bmatrix} = \begin{bmatrix} x_1 \\ y_1 \\ z_1 \end{bmatrix} + \begin{bmatrix} \alpha \\ \beta \\ \gamma \end{bmatrix} s, \quad 0 \leq s \leq l, \quad (32)$$

where x and y are horizontal positions, z is depth (m), (x_1, y_1, z_1) is the starting point of the line segment, α , β , and γ are the direction cosines of the line segment, and l is the length of the line segment (i.e., the distance the photon travels). The parametric equation for the solid cylinder describing the instrument (sensor head or buoy) is

$$\begin{bmatrix} x \\ y \\ z \end{bmatrix} = \begin{bmatrix} x_0 \\ y_0 \\ z_0 \end{bmatrix} + \begin{bmatrix} \rho \cos(\theta) \\ \rho \sin(\theta) \\ u \end{bmatrix}, \quad \begin{aligned} 0 &\leq \rho \leq r, \\ 0 &\leq \theta \leq 2\pi, \\ 0 &\leq u \leq h, \end{aligned} \quad (33)$$

where (x_0, y_0, z_0) is the location of the bottom center of the cylinder and r and h are the cylinder radius and height. The intersection points between the line coincident with the photon path and an infinite cylinder coincident with the cylinder wall satisfy

$$(x_1 - x_0 + \alpha s)^2 + (y_1 - y_0 + \beta s)^2 = r^2. \quad (34)$$

Equation (34) is quadratic in s , the solutions of which are

$$s = \frac{-B \pm \sqrt{B^2 - 4AC}}{2A}, \quad \begin{aligned} A &= \alpha^2 + \beta^2, \\ B &= 2\alpha(x_1 - x_0) + 2\beta(y_1 - y_0), \\ C &= (x_1 - x_0)^2 + (y_1 - y_0)^2 - r^2, \end{aligned} \quad (35)$$

and there exist intersection points if $(B^2 - 4AC) \geq 0$. Otherwise, for solutions s_1 and s_2 , the range of values of s for which the infinite line intersects an infinitely tall solid cylinder is $s_1 \leq s \leq s_2$. The finite photon path (of length l) is a subsegment of this infinite line. Values of s that satisfy $s \in \max(0, s_1) \leq s \leq \min(l, s_2)$ define the portion of the photon path that intersects the infinitely tall solid cylinder. If this range of s is finite, we find the boundaries of the corresponding range of u by substituting the limits of s into (from Eqs. (32) and (33))

$$u = z_1 - z_0 + \gamma s. \quad (36)$$

If this range of u overlaps $0 \leq u \leq h$ at any point, then the photon is known to hit the cylinder of height h .

In the modified BMC3D, ray-tracing calculations are performed both with and without the shading cylinder(s) in place. The power of the photons that exit the sea surface at each specified bin of solar zenith angles in the absence of shading is stored in the vector W , and the power of the photons that exit the sea surface at each specified bin of solar zenith angles in the presence of shading is stored in the vector W_s . Given the vector I that contains the angular shape of the illumination conditions, the sensor response in the absence of shading is given by Eq. (31). The sensor response with shading present is given by the dot product

$$L_u^m = W_s \bullet I. \quad (37)$$

The overall fractional shading error, as computed by the modified BMC3D, is

$$\mathcal{E} = \frac{W \bullet I - W_s \bullet I}{W \bullet I}. \quad (38)$$

3.2 Ray-tracing Data Tables

For each set of instrument dimensions investigated, data tables of W and W_s were generated in one (or both) of two ways. One approach is to choose a list of values for each input (a , b/a , etc.) and then compute W and W_s for each permutation of inputs, creating an ordered table of results that can be easily interpolated. The second approach is to compute results for random values of the inputs, creating data that can be used to train a neural network. In either case, we generated separate tables for optically deep water and for shallow water. In all cases we chose to compute azimuthally averaged results at nine solar zenith angles. (Because our instrument and sensor are azimuthally symmetric, there would be nothing gained if we retained the azimuthal dependence of the ray tracing results.)

The ordered deepwater table, which we call `wsum3.dat`, has four lines of header information. Line 1 contains a title. Lines 2 through 4 are led by a negative integer. The minus sign is a flag for our computer codes identifying the line as a header line. The integer identifies the number of entries for the parameter listed on that line; these are followed by the values of the parameters. Line 2 lists the solar zenith angles (9), line 3 the values of a , line 4 the values of b/a . Each data row, which represents the results of one MC simulation, has at least 20 columns: 9 columns of W results, from 82.5 degrees down to 0 (82.5, 70, 60, ... 20, 10, 0); 9 columns of W_s results (from 82.5 to 0); and the values of a and b/a . Additional columns of information can be added, such as the number of photons (N) used in the simulation. The rows are ordered such that we set b/a to its smallest value, cycle through all values of a for this value of b/a , increment b/a , and cycle through all a values, etc. New data cannot be added to the table for only one set of values at a time; if one wishes to add data for a new value of a , for example, data must be added for that value of a for every value of b/a that exists in the table.

The ordered shallow-water table, `wsum5.dat`, has six lines of header information. Line 1 is a title. Analogous to the deepwater table, the next 5 lines are led by a negative integer indicating the number of values for each parameter, followed by the parameter values. Line 2 lists the Sun angles (9) used, line 3 lists the values of a , line 4 lists the values of b/a , line 5 lists the values of a^*z , and line 6 lists the values of R_b . Each data row has at least 22 columns: 9 columns of W data, from 82.5 deg down to 0; 9 columns of W_s (from 82.5 to 0); and the values of a , b/a , a^*z , R_b . Again, additional columns of information can be added, such as the number of photons (N) used in the simulation. The rows are ordered such that we cycle through all values of a for each value of b/a , cycle through all values of b/a for each value of a^*z , and cycle through all values of a^*z for each value of R_b (i.e., R_b increments the slowest, followed by a^*z , b/a , and a). New data cannot be added to the table one at a time; if one wishes to add data for a new value of a , for example, data must be added for that value of a for every combination of b/a , a^*z , and R_b that exists in the table.

Figure 23 shows the process for the creation and use of the `wsum3` and `wsum5` data tables for ordered simulations. The FORTRAN code `wsumgen.f` is modified to include the lists of parameters (i.e., values of a , b/a , etc.). The code is compiled (with Lahey/Fujitsu Fortran 95 Express) and executed to produce the output file `wsumgen.out` that contains W and W_s values. If necessary, these output values are added to previously existing output values and properly sorted in Excel (Microsoft, Inc. Redmond, Washington). Header information is added that includes the values of the parameters for the overall data

table and the data table is saved to a text file Wsum3.dat or Wsum5.dat. These text files can be read by the Matlab code Wsumplot.m in order to generate plots of the data, and they can be read by our Hyper-TSRB data correction code shade_c.f, which is described later.

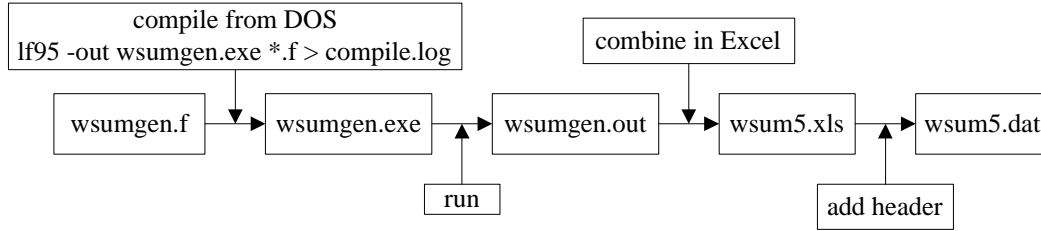


Fig. 23 — Generating or expanding the ordered Monte Carlo data tables

The randomized table, wsumbp.dat, need not contain any header information. Each data row has at least 22 columns: 9 columns of W data, from 82.5 degrees down to 0; 9 columns of W_s data (from 82.5 to 0); and the values of a , b/a , a^*z , and R_b .

Our initial approach was to refine the wsum3.dat and wsum5.dat tables with a large number of Monte Carlo simulations and then use linear interpolation of the tables to determine the shading error for any set of parameters (e.g., a and b). This was fairly successful for deepwater computations, but it proved to be problematic for shallow-water computations. Monte Carlo noise makes it difficult to generate a data table that is smooth in five dimensions. Because of the difficulty of smoothing a sparsely populated five-dimensional table, we decided to also try to generate random-input data for more inputs but fewer photons and to use the results to train a neural network. This is described in the next section. For this purpose, we computed a large number of Hyper-TSRB W and W_s vectors for random values of water and seafloor properties (the wsumbp.dat file described above). Because additional inputs to this table are random, any number of new ray-tracing results can be added at any time, making it easy to reduce the Monte Carlo noise.

3.3 Post-processing of the Ray-tracing Results

The ray-tracing results were manipulated in three ways. First, we found it prudent to convert the W and W_s vectors to ϵ_{Sun} and \tilde{W} vectors, where ϵ_{Sun} contains shading error values for direct sunlight (and no skylight) and \tilde{W} is a normalized version of W ,

$$\tilde{W}_i \equiv \frac{W_i}{\sum_i W_i},$$

where each W_i is the power of the photons exiting the sea surface for the i^{th} solar zenith angular bin. The ordered data files are normalized using our Matlab code mk_erwn.m, which creates the output files erwn5.dat and erwn5.mat. Then, in the case of random-input ray-tracing results, we trained a neural network with the ϵ_{Sun} and \tilde{W} vectors and used the resulting network to construct a well-behaved data table of ϵ_{Sun} and \tilde{W} vectors for specified values of a , b/a , a^*z , and R_b . Finally, for all tables we used theoretical limits wherever possible to bound the values in the table. Each of these three steps is explained in more detail below.

Expanding Eq. (38),

$$\mathcal{E} = \frac{\sum_i W_i I_i - W_{si} I_i}{\sum_i W_i I_i}. \quad (39)$$

If we let \mathcal{E}_i , W_i , and W_{si} denote elements of \mathcal{E}_{Sun} , W , and W_s , respectively, then the black-sky error for a particular solar zenith angle is given by

$$\mathcal{E}_i \equiv \frac{W_i I_i - W_{si} I_i}{W_i I_i} = \frac{W_i - W_{si}}{W_i}. \quad (40)$$

Rearranging,

$$W_{si} = (1 - \mathcal{E}_i) W_i. \quad (41)$$

Substituting Eq. (41) into Eq. (39),

$$\mathcal{E} = \frac{\sum_i W_i I_i - (1 - \mathcal{E}_i) W_i I_i}{\sum_i W_i I_i} = \frac{\sum_i \mathcal{E}_i W_i I_i}{\sum_i W_i I_i}. \quad (42)$$

Note that the W_i values in Eq. (42) can be normalized by the sum of W_i without changing the result. We can therefore rewrite Eq. (42) as

$$\mathcal{E} = \frac{\sum_i \mathcal{E}_i \tilde{W}_i I_i}{\sum_i \tilde{W}_i I_i} \quad (43)$$

Post-processing of the random-input Monte Carlo results (wsumbp.dat) is done with our Matlab program (wsumbp.m) using the Matlab Neural Networks toolbox. Two separate neural networks are generated, one (e.g., net_err5.mat) that computes \mathcal{E}_{Sun} and one (e.g., net_wn5.mat) that computes the normalized form of the nine-value W vector (ray-tracing result in the absence of shading).

For the Hyper-TSRB, we constructed both networks to have eight nodes in the input layer, five nodes in a hidden layer, and one node in the output layer. These sizes were chosen somewhat arbitrarily; we want to have just enough nodes to ensure good results without making the network unnecessarily large. The tansig function was used for all nodes. Back-propagation training of the network was done with Matlab's 'trainlm' routine, which is based on Levenberg-Marquardt optimization [29]. The input to the shallow-water networks is the vector $[\theta_0; a; b/(a+b); (a^*z); R_b]$ normalized such that each input is limited to the range 0 to 1. Eighty percent of the wsumbp.dat entries were used to train the networks, the other 20% to test their performance. Training was continued until the performance of the test set started to degrade.

For all of our ray-tracing data tables, we looked for theoretical limits that enable us to either bound the table or remove outliers. The biggest advantage of converting W and W_s to ϵ_{Sun} and \tilde{W} is that we know that $0 < \epsilon_{\text{Sun}} < 1$ and $0 < \tilde{W} < 1$. In addition to these limits, we can set $\epsilon_{\text{Sun}} = 1$ when $z_{\text{bot}} - z_s = 0$, $\epsilon_{\text{Sun}} = 0$ when $a = 0$, and $\epsilon_{\text{Sun}} \rightarrow 1$ as $a \rightarrow \infty$.

Figure 24 summarizes the post-processing flow for the ordered and random numerical simulations as well as for the analytical analysis. The `shade_c.m` and `shade_plot.m` elements in Fig. 24 are used to correct instrument data and to generate plots for analysis. They are both described in greater detail later in this document.

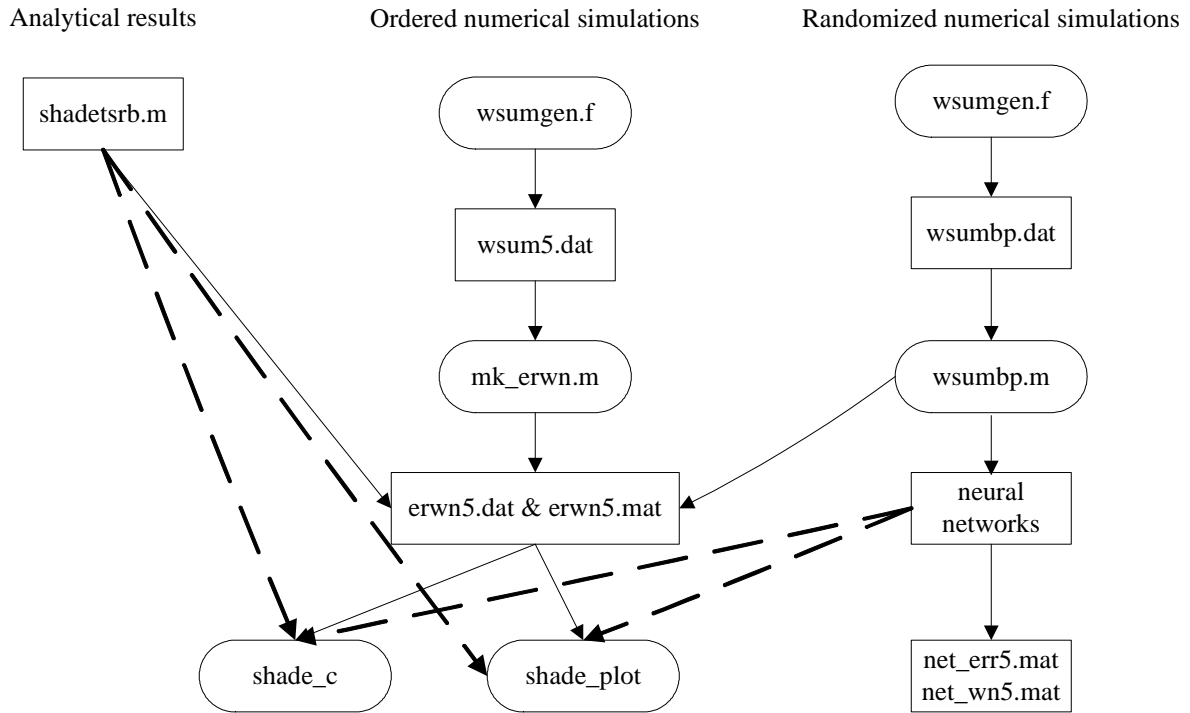


Fig. 24 — Ray tracing simulation data flow. Dotted lines are optimal paths for data processing.

3.4 Results for a Non-buoyed Radiometer

In a properly coded Monte Carlo computation, the standard deviation in the result due to statistical noise is proportional to $N^{-1/2}$, where N is the number of photons collected. As a test of the modified BMC3D code, we ran a simulation for a two-dimensional shading disk with 10^4 , 10^5 , 10^6 , and 10^7 photos, ten times each (with different initial seeds for the random-number generator) and plotted the standard deviations for the groups of ten runs. As shown in Fig. 25, the standard deviation followed the expected $N^{-1/2}$ pattern, verifying that we need to increase the number of photons by two orders of magnitude in order to reduce the statistical noise by one order of magnitude.

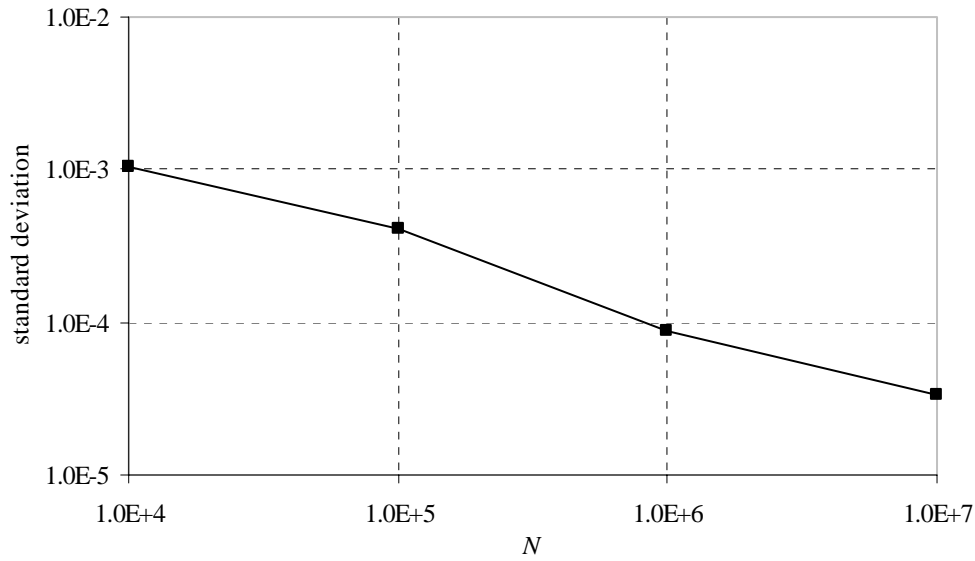


Fig. 25 — Convergence of standard deviation of backward Monte Carlo simulations for a shading disk

Equation (13) gives an analytical approximation to the shading error of a cylindrical upwelling radiometer. Gordon and Ding [8] extend the usefulness of this approximation by retaining its functional form [i.e., Eq. (1)] but obtaining values of k numerically using backward Monte Carlo simulations. They do this both for L_u and E_u sensors placed just below the surface and for various illumination conditions, but only for optically deep waters. Using the k values from Table 1, Eq. (1) gives shading error relationships that look similar to those shown in Figs. 6 and 7 but that differ somewhat in magnitude.

To compare results from our modified BMC3D code with those reported by Gordon and Ding, we computed the shading error caused by a two-dimensional disk on upwelling irradiance (E_u) for an idealized clear sky and solar zenith angle of 70 deg. Shown in Fig. 26 are results from BMC3D for 10^6 photons and five values of the product of a and r compared with results from Gordon and Ding. The agreement is satisfactory, given the statistical uncertainty of both our results and those of Gordon and Ding. Since buoyed radiometers are our primary interest, we did not pursue the shading disk case any further.

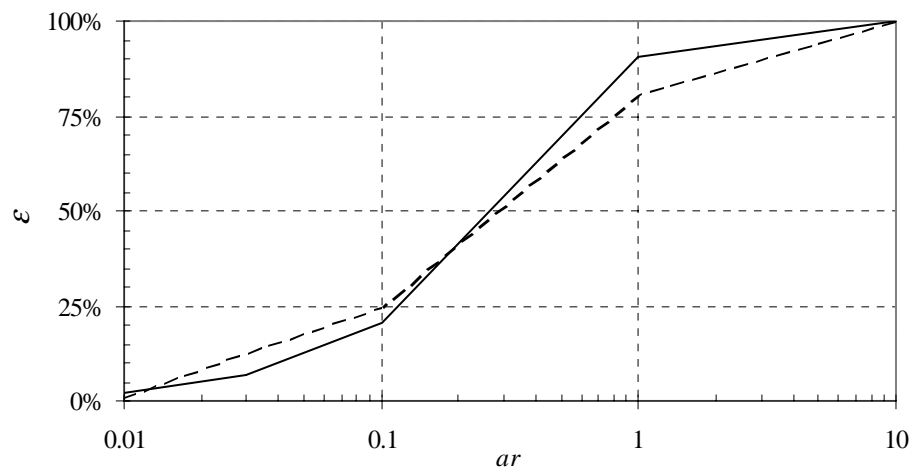


Fig. 26 — Results of error vs (ar) for Gordon's method (solid) compared to the MC method (dashed) for a Sun angle of 70°

Doyle [17] provides some Monte Carlo results for a vertical cylinder, in which the height of the instrument was taken into account. These simulations are for a cylinder 1 m tall and for several different viewing angles. The results show that when the viewing angle is nadir, the cylinder height has insignificant effect on the shading. Our modified BMC3D code cannot simulate abovewater shading; however, we can simulate the shading of a submerged cylindrical instrument. Our preliminary computations of shading error for a single cylinder were very similar to those for two-dimensional disk of the same radius, confirming Doyle's results.

3.5 Results for the Hyper-TSRB in Deep Water

Deepwater simulations of Hyper-TSRB shading were performed with the modified BMC3D code for various values of water absorption and scattering coefficients. The Fournier-Forand scattering phase function [30] was used with its two parameters set to $n = 1.10$ and $\mu = 3.62$. These parameters give a close fit to the Petzold San Diego Harbor scattering phase function [31] but with a 25% improved run-time efficiency. Some of the results from these simulations have already been reported by Leathers, Downes, and Mobley [32].

Table 6 lists the Hyper-TSRB shading error for undisturbed, optically deep water both for a diffuse sky and for a Sun in a black sky at eight solar zenith angles. Results are shown for six values of a and, for $\theta_0 < 20$ deg, three values of b/a . For $\theta_0 > 20$ deg, the dependence on b was found to be insignificant and the results shown in Table 6 are those for $b/a=1, 2$, and 4 averaged together. Estimates of the statistical uncertainty in the error values, derived from the standard deviation of the simulations, is provided for the smallest and largest values of a .

Table 6 — Percent Shading Error ($100 \times \varepsilon$) of a Hyper-TSRB for Given Values of Absorption Coefficient a , Scattering Coefficient b , and Solar Zenith Angle θ_0

θ_0 (deg)		$a=0.02 \text{ m}^{-1}$	0.05	0.1	0.2	0.5	1.0
0	$b/a = 1$	$6.1 \pm 0.6\%$	11.7	22.0	35.8	55.5	69.5 ± 1.4
	2	6.0 ± 0.7	11.1	20.8	33.3	49.3	58.1 ± 1.0
	4	5.9 ± 0.8	11.0	18.0	26.3	37.3	43.0 ± 0.5
10	$b/a = 1$	3.2 ± 0.3	7.6	13.1	21.6	39.9	53.6 ± 0.5
	2	3.2 ± 0.2	6.9	12.3	20.4	35.0	46.5 ± 0.4
	4	2.6 ± 0.3	6.4	11.0	17.7	28.6	36.8 ± 0.3
20	$b/a = 1$	0.6 ± 0.2	2.0	4.4	8.2	17.4	29.8 ± 0.4
	2	0.9 ± 0.2	2.2	4.1	7.6	17.3	28.8 ± 0.4
	4	1.0 ± 0.3	2.0	4.3	7.7	16.4	26.3 ± 0.2
30	$b/a = 2$	0.5 ± 0.1	1.2	2.2	4.9	11.3	20.9 ± 0.2
40	$b/a = 2$	0.5 ± 0.1	0.7	1.8	3.5	8.8	16.4 ± 0.1
50	$b/a = 2$	0.1 ± 0.1	0.6	1.1	2.8	6.9	13.9 ± 0.1
60	$b/a = 2$	0.2 ± 0.1	0.6	1.0	2.4	6.1	12.1 ± 0.1
70	$b/a = 2$	0.0 ± 0.1	0.7	1.1	2.3	5.3	11.2 ± 0.2
diffuse	$b/a = 1$	0.5 ± 0.1	1.3	2.6	5.1	11.4	20.0 ± 0.2
	2	0.6 ± 0.1	1.4	2.5	4.9	10.9	19.4 ± 0.2
	4	0.5 ± 0.1	1.5	2.4	4.7	10.2	18.4 ± 0.1

Figure 27 shows the shading error vs a for optically deep water, $b/a = 2$, and five solar zenith angles (θ_0) for a Sun in a black sky. For large values of θ_0 , the error increases approximately linearly with a (over the range studied), whereas for smaller Sun angle, and therefore larger shading errors, the error depends on a in a nonlinear manner. Shown in Fig. 28 is a comparison of Monte Carlo results with values of shading error predicted by Eq. (1) using $r = 0.045 \text{ m}$ (sensor head radius) and the numerically derived values of k provided by Gordon and Ding (Table 4). Equation (1) was found to give a good fit to the data for large solar zenith angles ($\theta_0 > 40 \text{ deg}$). For moderate solar zenith angles ($20 \text{ deg} < \theta_0 < 40 \text{ deg}$), Eq. (1) gives good results for small values of ($a r$), but overestimates the error for large values of ($a r$). For small values of θ_0 , where the effect of the buoy is significant, Eq. (1) significantly underestimates the error at low values of a and overestimates the error at high values of a . Note that Eq. (1) cannot provide a result for $\theta_0 = 0 \text{ deg}$.

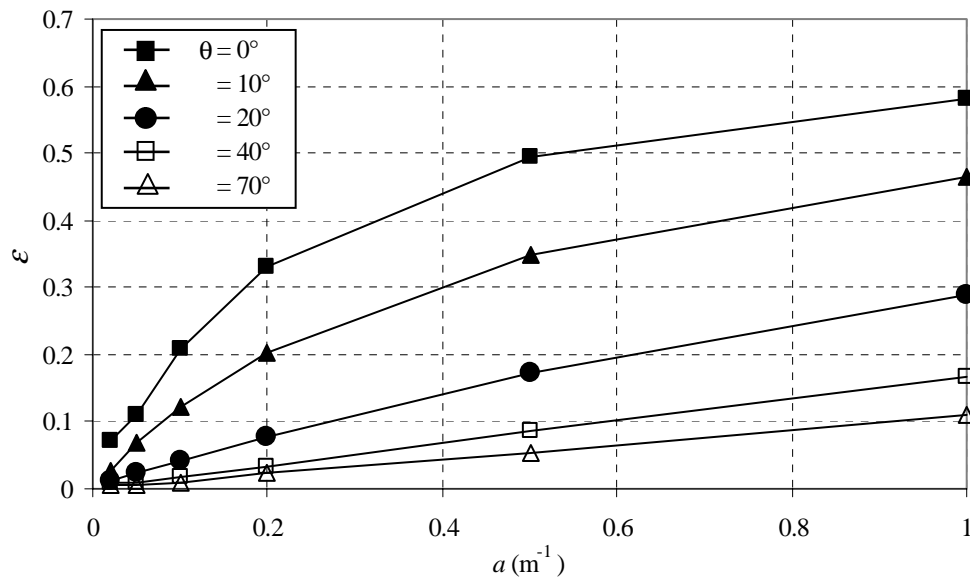


Fig. 27 — Self-shading error of the Hyper-TSRB in deep water for $b/a=2$, five solar zenith angles, and no diffuse skylight

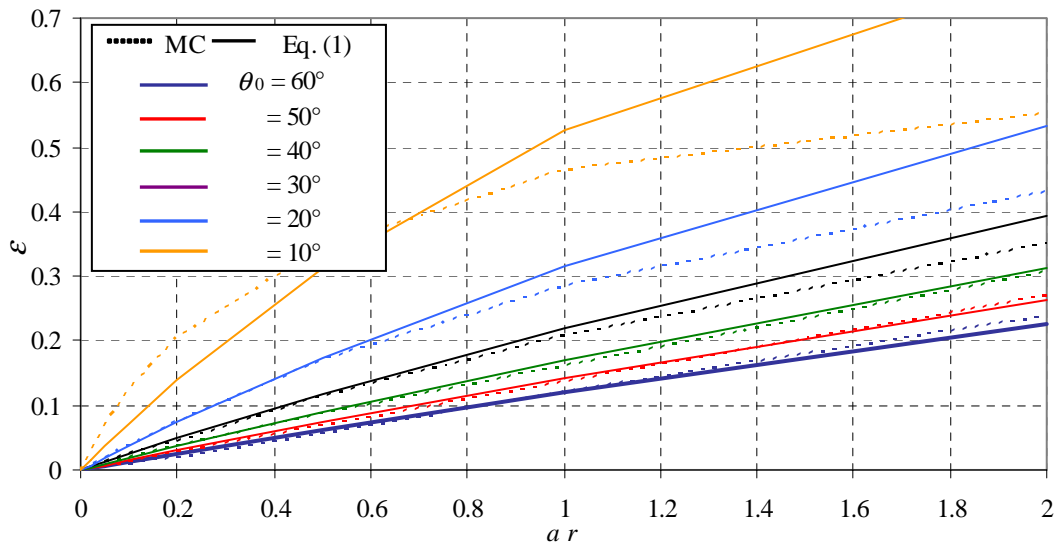
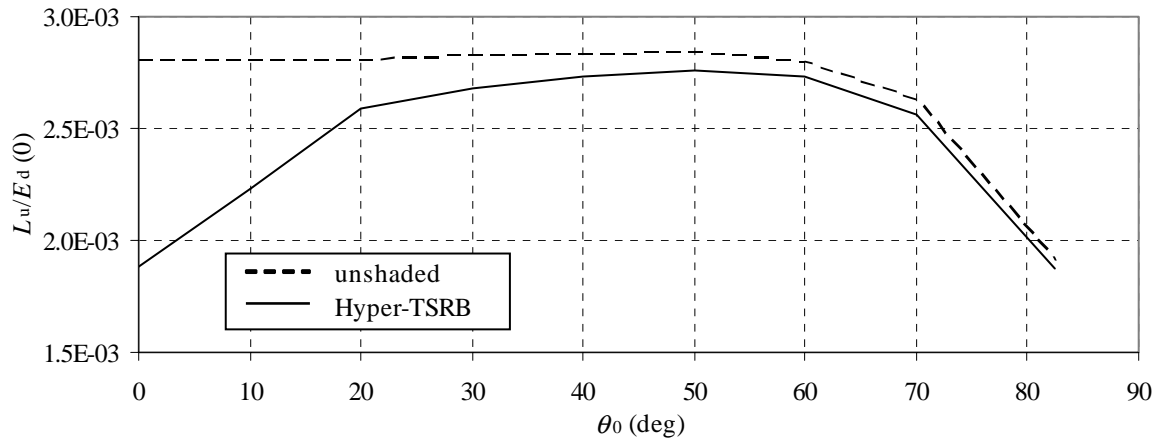


Fig. 28 — Comparison of Monte Carlo results with Eq. (1)

As already seen in Fig. 27, self-shading error depends strongly on Sun position. The top plot in Fig. 29 shows the upwelling radiance L_u vs solar zenith angle both with the Hyper-TSRB present and in its absence. These simulations are for a Sun in a black sky, optically deep water, and $a = b = 0.2 \text{ m}^{-1}$. The values of L_u shown in Fig. 29 are normalized by the downward irradiance at the sea surface $E_d(0)$. The shading error, shown in the bottom plot of Fig. 29, is large for small Sun angles and small for large Sun angles. Here, too, we see that the Hyper-TSRB shading error in deepwater lies between those predicted by Eq. (1) for the radii of the Hyper-TSRB sensor body and buoy. Also shown in Fig. 29 is the error due to the main body of the Hyper-TSRB without the buoy. It can be seen that the buoy has a large effect, but only for $\theta_0 < 20$ deg. This was found to be true in general, and therefore the shading error of the Hyper-TSRB has a much stronger dependence on θ_0 than does that of a nonbuoyed cylindrical instrument.

Figure 30 shows the Hyper-TSRB shading error vs solar zenith angle for a Sun in a black sky, six values of a , and $b/a=2$. For all values of a , the shading error is significant at small values of θ_0 and decreases with increasing θ_0 . Figure 31 compares our Monte Carlo results for the Hyper-TSRB and $b/a = 0.5$ with our analytical model for a buoyed radiometer (Eq. (21)). Although, as expected, the analytical model does not give good values for the special case of $\theta_0 = 0$ deg, it performs very well for all the other solar zenith angles. This is a very important result; Eq. (21) will be very valuable to the ocean optics communities if it can provide accurate estimates of self-shading for a buoyed radiometer with any set of dimensions (i.e., r_s , r_b , and z_d).

a)



b)

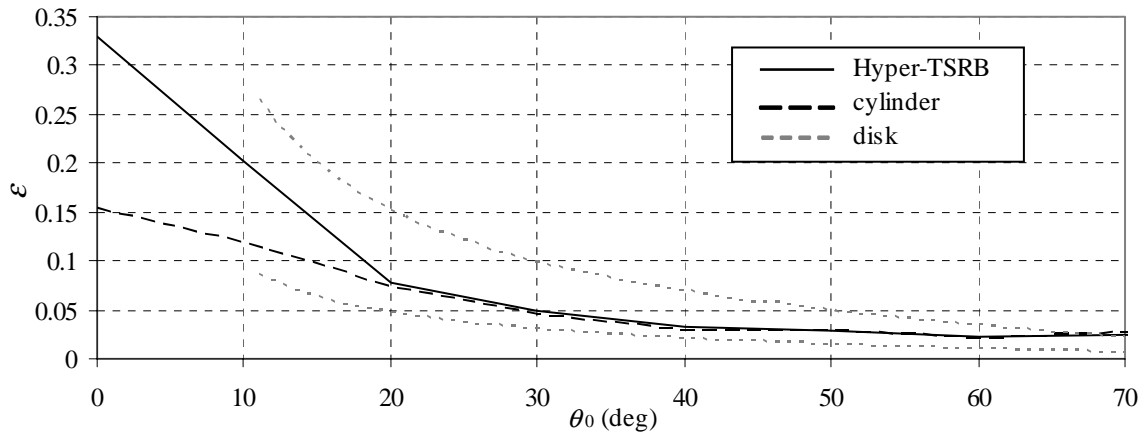


Fig. 29 — Shaded and unshaded normalized radiance (a) and percent shading error (b) of the Hyper-TSRB and of the Hyper-TSRB cylindrical body without the buoy compared with Eq. (1) for radii 0.044 m and 0.15 m. These computations are for a Sun in a black sky, deep water, and $a = b = 0.2 \text{ m}^{-1}$.

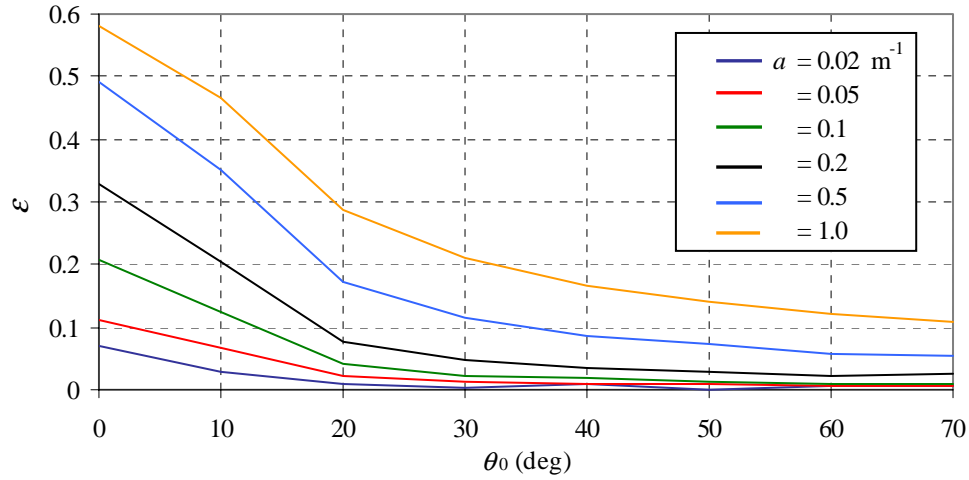


Fig. 30 — Percent shading error of the Hyper-TSRB in deepwater vs solar zenith angle θ_0 for the Sun in a black sky, six values of a , and $b/a = 2$

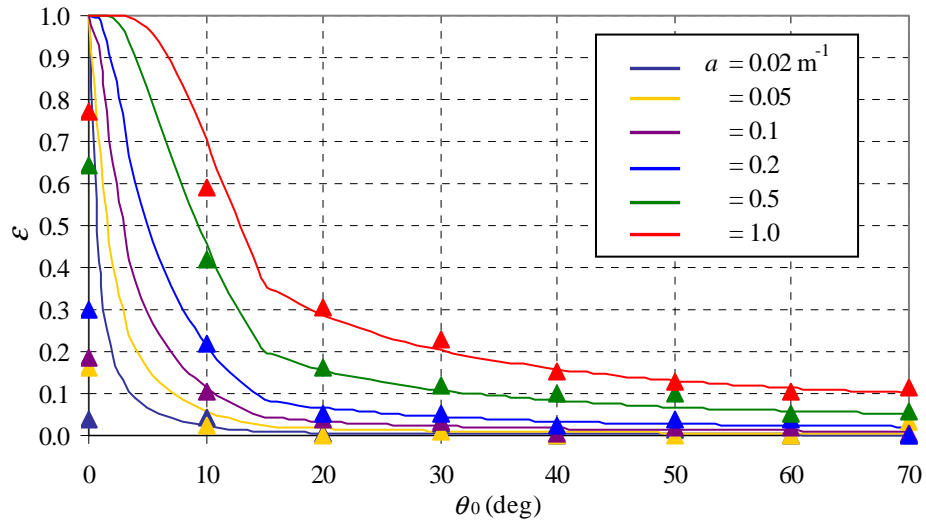


Fig. 31 — Self-shading error of the Hyper-TSRB as predicted by Eq. (24) compared with results from MC simulations (triangles) for $b/a = 0.5$

For a given value of a the shading error in optically deep water is generally smallest for large values of b because scattering enables the regions shadowed from direct light to be filled in with scattered light. However, we found this effect to be significant only for small values of θ_0 , where the shading effect is greatest. This is likely because shading at small solar zenith angles is dominated by shading from the buoy, which is more easily counteracted by scattering since the buoy is vertically separated from the sensor. Shown in Fig. 32 is the Hyper-TSRB shading error vs b for $\theta_0 = 0, 10$, and 20 deg, each for $a = 0.2, 0.5$, and 1.0 m^{-1} . It can be seen that the slope of shading error curves are similar for constant θ_0 but that this slope decreases with increasing θ_0 .

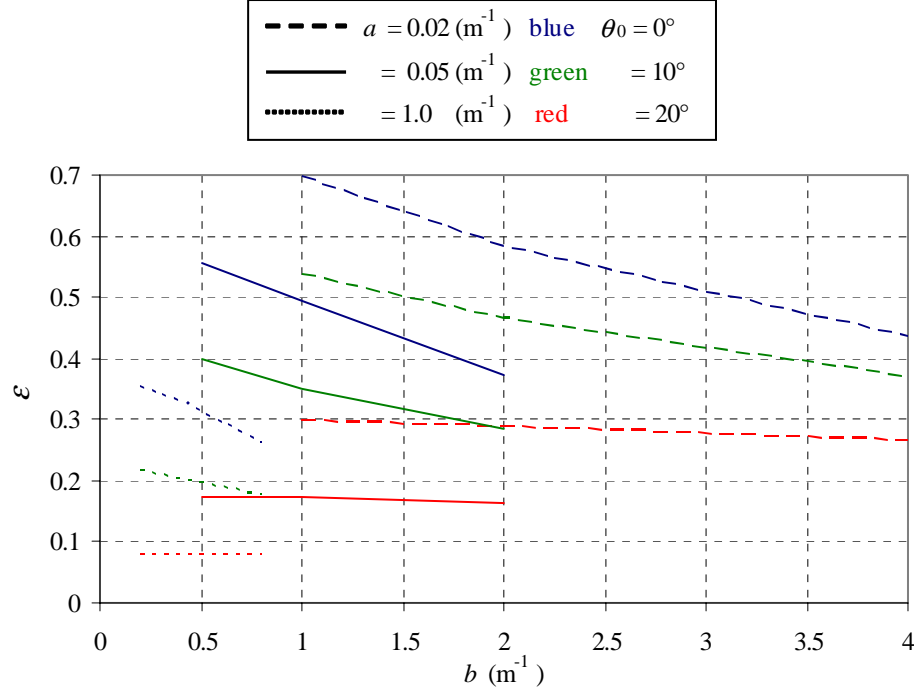


Fig. 32 — Percent shading error of the Hyper-TSRB in deepwater for $a = 0.02 \text{ m}^{-1}$ (dashed), 0.05 m^{-1} (solid), and 1.0 m^{-1} (dotted) and $\theta_0 = 0 \text{ deg}$ (top, blue), 10 deg (middle, green), and 20 deg (bottom, red)

We can develop a semianalytical model to account for the effect of scattering. From Eq. (18),

$$\varepsilon = 1 - \exp\left[-\left(1 + 1/\cos\theta_{0w}\right)a(z_0 - z_s)\right], \quad (44)$$

where $z_0 = r_d / \tan\theta_{0w}$. But because the depth of the shadow, z_0 , is reduced by scattering, we can replace z_0 in Eq. (44) with the reduced shade depth value z_0' ,

$$z_0' = r_d \exp(-k_1 b z_0), \quad (45)$$

where r_d is the radius of the shading disk (sensor head or buoy). Shown in Fig. 33 is the self-shading error as computed with Eqs. (44) and (45) for $k_1 = 0.1$. This gives a good model for the effect of scattering on self-shading; however, the value of k_1 had to be determined numerically based on the results of the Monte Carlo simulations.

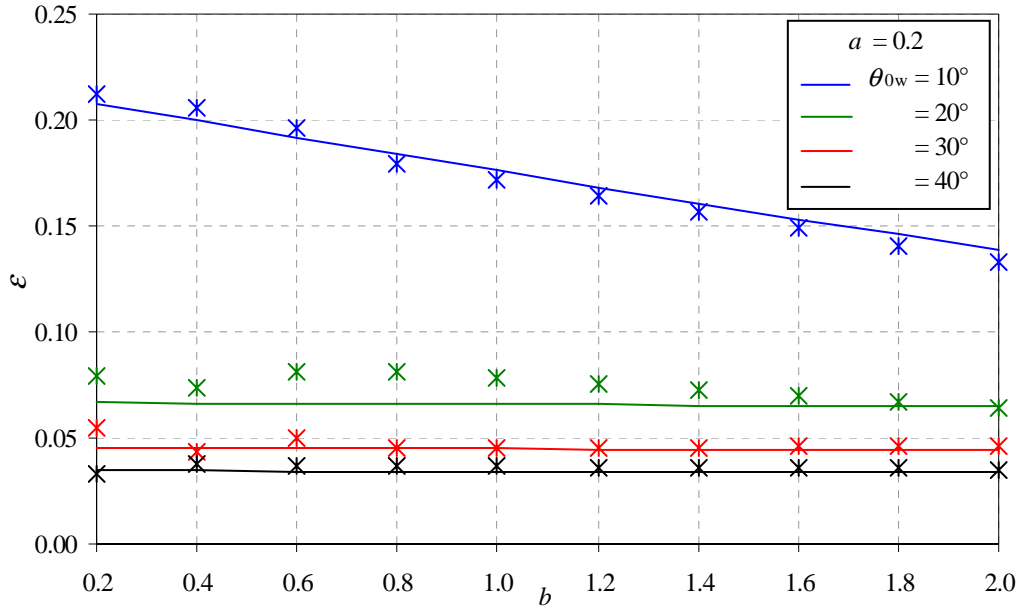


Fig. 33 — Hyper-TSRB self-shading vs scattering coefficient for $k_1 = 0.01$ and $a = 0.2 \text{ m}^{-1}$. Semianalytical values (solid lines) were obtained with Eqs. (44) and (45), and numerical results (*) were computed with BMC3D.

3.6 Results for the Hyper-TSRB in Shallow Water

Figures 34 and 35 show the Hyper-TSRB shading error vs total water depth (z_{bot}) for several different Sun positions. In both figures, $b/a = 2$ and $R_b = 0.2$; in Fig. 34 $a = 0.2 \text{ m}^{-1}$, and in Fig. 35 $a = 0.5 \text{ m}^{-1}$. Note that the Hyper-TSRB upwelling radiance sensor is 0.66 m below the surface, so the distance the sensor is from the seafloor is $(z_{\text{bot}} - 0.66)$. The solid lines are the values obtained with the complete analytical model described in Section 2. The point data were obtained from BMC3D simulations with 10^7 photons. In Fig. 35 we have included the self-shading error predicted by a trained neural network. In very shallow water, the radiance measurement is dominated by the component of light being reflected off the seafloor. If the instrument is very close to the seafloor, it mostly sees its own shadow. As the water depth is increased (i.e., the instrument is moved further from the bottom), the shading error in the radiance reflected off the bottom decreases, as does the overall shading error. However, as the water depth is further increased, the water-column component of the upwelling radiance begins to dominate and the overall shading error increases toward the optically deep values. We reported this general shape of shading error vs depth in Ref. 32. (However, in the specific example we provided, the values of shading error near the bottom were incorrectly low.)

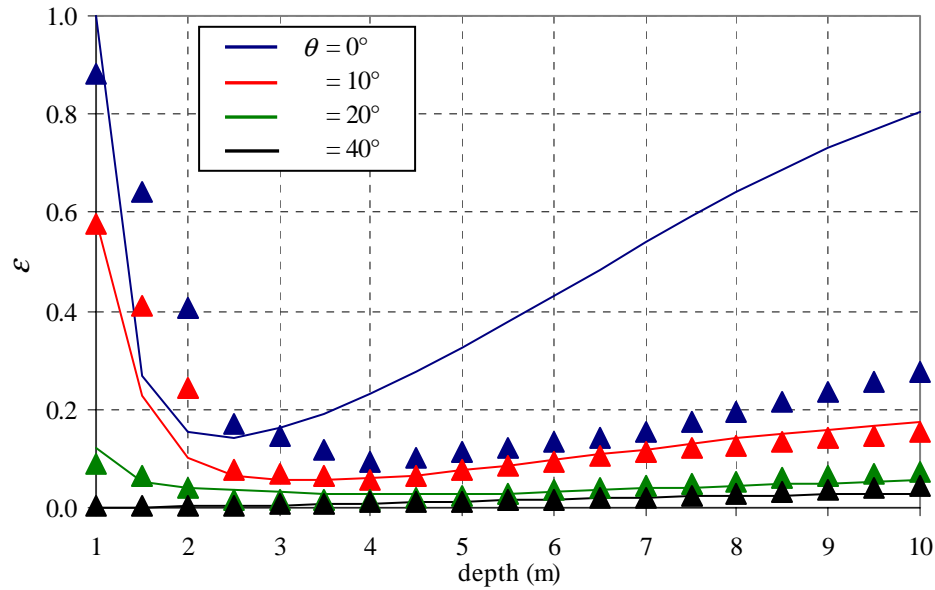


Fig. 34 — Hyper-TSRB shading error as predicted with the analytical model compared with MC results (triangles). Shown are results for $a = 0.2 \text{ m}^{-1}$, $b = 0.4 \text{ m}^{-1}$, $R_b = 0.2$, FOV half-angle = 20 deg, and four values of the solar zenith angle.

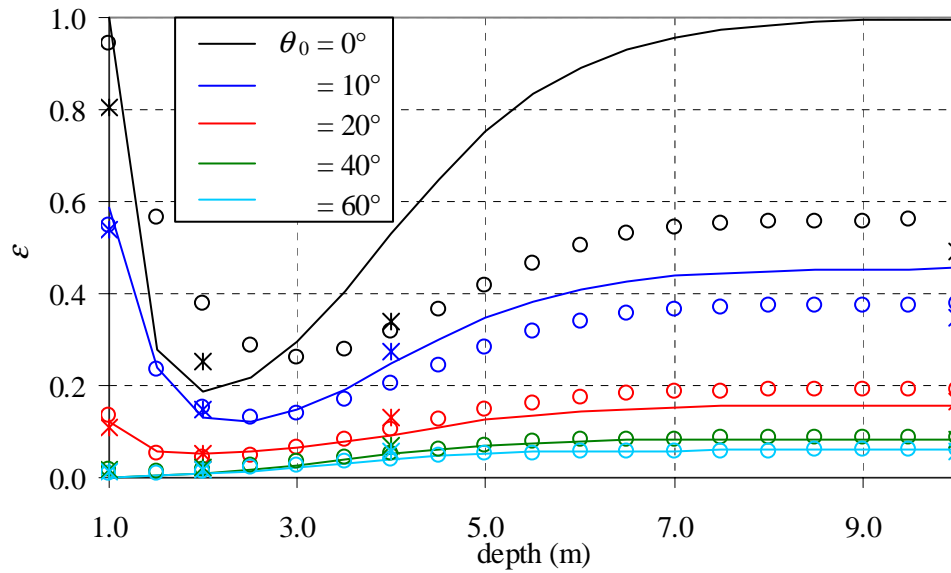


Fig. 35 — Hyper-TSRB shading error as predicted with the analytical model (solid lines) compared with MC results (asterisks) and neural network predictions (circles). Shown are results for $a = 0.5 \text{ m}^{-1}$, $b = 0.4 \text{ m}^{-1}$, $R_b = 0.2$, FOV half-angle = 20 deg, and nine values of the solar zenith angle.

The agreement between the model and the numerical results in Figs. 34 and 35 is much better than what first meets the eye. The top curve in each figure is for $\theta_0 = 0$ deg. For this special case, k is infinite in the water-column portion of the analytical model, and, as pointed out by Gordon and Ding [8], the model breaks down, giving a result of 100% error in L_{uw} . Therefore, although our overall analytical

model gives good estimates of Hyper-TSRB shading for $\theta_0 = 0$ deg close to the seafloor, it greatly overestimates the shading error far from the seafloor. Although this is of academic interest, it should be kept in mind that the real-life situation of $\theta_0 = 0$ deg is rare, and L_u measurements for very small values of θ_0 should be avoided. The agreement between the analytical and numerical results for solar zenith angles of 10 deg and greater is very good. (Keep in mind that the numerically derived values contain some Monte Carlo uncertainty, which for 10^7 photons is significant.) The only data points in the two figures that seem to have significant disagreement are those at 10 m for $a = 0.5 \text{ m}^{-1}$ and $\theta_0 = 10$ deg. This is due at least in part to the deepwater analytical model's limitation to relatively small values of $(a r)$ when $\theta_0 < 20$ deg [8]. However, because solar zenith angles of 10 deg or smaller will not typically be encountered in ocean optics field experiments, this discrepancy should not be an issue. If one requires shading results for the combination of large a and small θ_0 , then it will be necessary to construct a semianalytical model that uses numerically derived water-column-component shading values for a and small θ_0 .

Our analytical model enables us to quickly model situations for which we have not run numerical simulations. For example, we can investigate the dependence of shading on the size of the buoy and on the vertical distance between the buoy and sensor. Shown in Fig. 36 is the shading error of the Hyper-TSRB as a function of buoy radius for several different total water depths. When the radius is very small, the shading is determined by the sensor-head cylinder, and the size of the buoy does not matter. Once the buoy is large enough to influence the overall shading, there is an approximately linear relationship between buoy radius and shading.

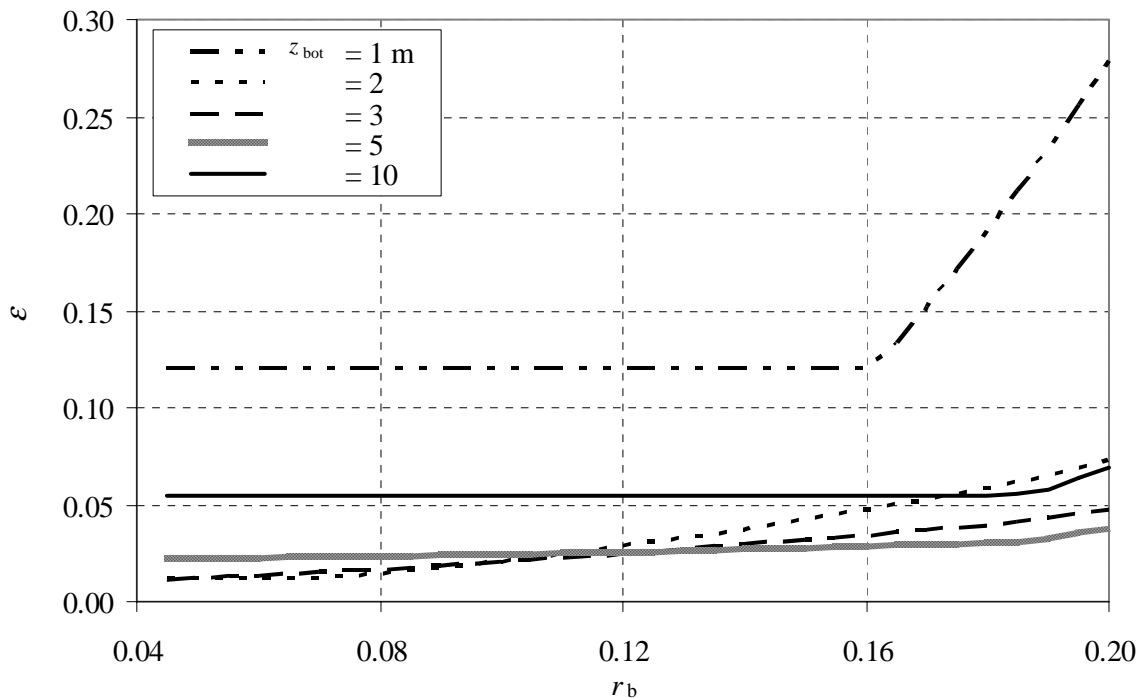


Fig. 36 — Hyper-TSRB self-shading error vs buoy radius for several different water depths ($a = 0.2 \text{ m}^{-1}$, $\theta_0 = 20$ deg)

4. RADIOMETER DATA CORRECTION

4.1 Correction Algorithm

We have written a FORTRAN program, `shade_c.f`, that applies a self-shading correction to upwelling radiometer data. The program uses a table look-up approach that reads and interpolates a table of W and W_s vectors that were generated with the Monte Carlo code. Based on the user's input, the program reads either a deepwater table of the format of `wsum3.dat` (described in Section 3) or a shallow-water table of the format of `wsum5.dat`. Interpolation of `wsum3.dat` or `wsum5.dat` is based on the water depth and on user-supplied data files that contain wavelength-dependent values of the a , b , and R_b . At run time, the user also supplies information about the illumination conditions, and the program computes the vector I . The total shading error is computed with Eq. (38).

The `shade_c` program contains nothing that is specific to a particular instrument. The shading information is contained in the `wsum3.dat` and `wsum5.dat` data files, which are supplied at runtime. The data files `wsum3.dat` and `wsum5.dat` can be built entirely from numerically simulated results or entirely from analytically derived values or some mixture of the two. For our Hyper-TSRB study, we are using `wsum3.dat` values that are direct results from the numerical simulations and `wsum5.dat` values that were computed by the neural network trained on simulated results.

The files required to compile the correction code are `shade_c.f`, `readLu.f`, `readRb.f`, and the five interpolation routines `lin5to4.f`, `lin4to3.f`, `lin3to2.f`, `lin2to1.f`, and `lin1to0.f`. We compile the code using Lahey/Fujitsu Fortran 95 Express. Provided that all the required files are present in the current directory (and no other *.f files are present), the program can be compiled with the command

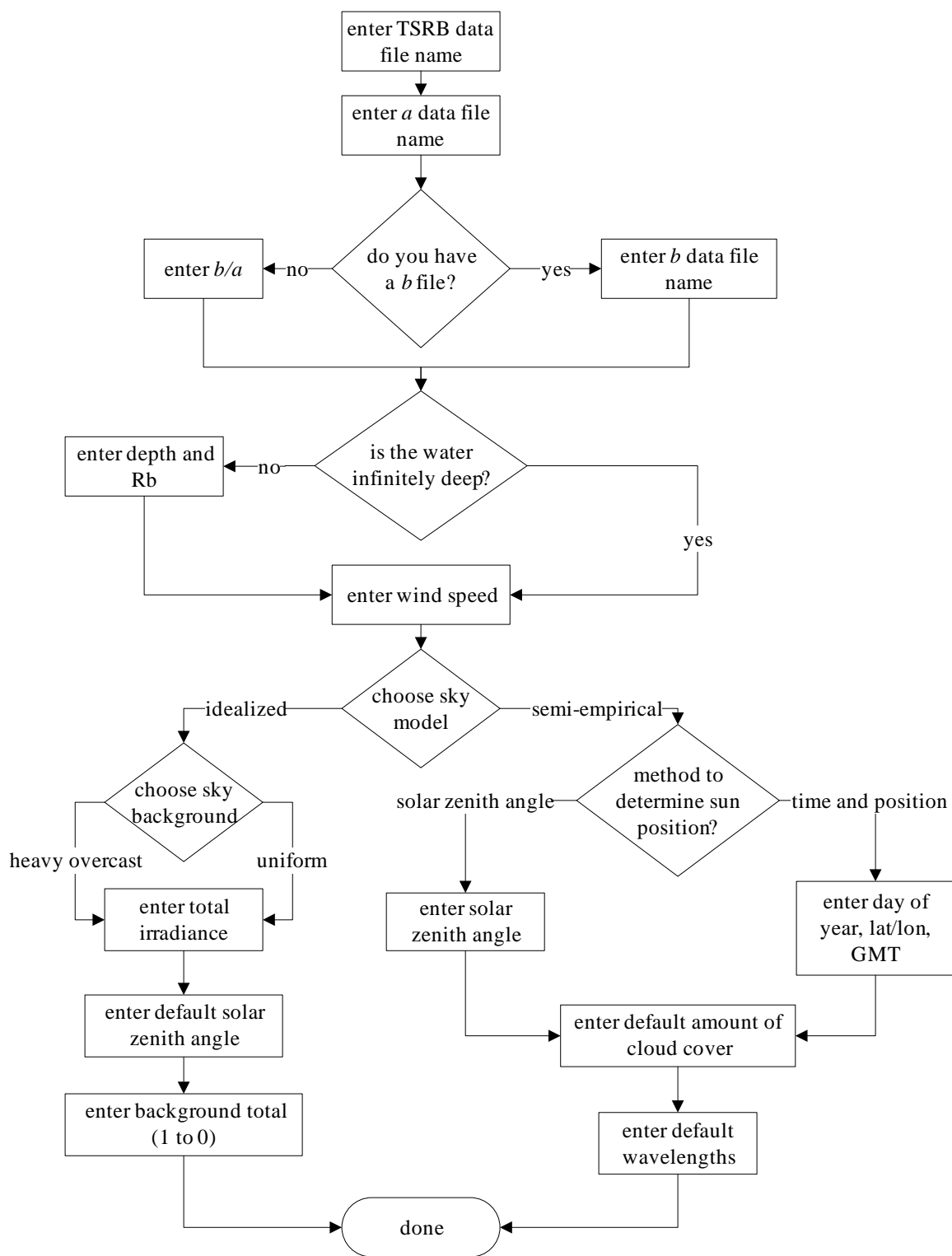
```
> lf95 -out shade_c.exe *.f > compile.log .
```

To run the executable, the following files are required: `wsum3.dat`, `wsum5.dat`, a file of Hyper-TSRB data as a function of wavelength, a file of absorption data as a function of wavelength, and a file of bottom albedo data as a function of wavelength. A backscatter coefficient file as a function of wavelength is optional: values for b may be chosen as multiples of the absorption coefficient data. Running `shade_c.exe` also requires `gcirrad.txt` (data for the Gregg and Carder [26] sky irradiance model) and a defaults file, which is a file of default settings used for input to the program. Note that the default values do not need to be set before program execution as the user is given the option of entering new values as the program is running. If the new values are not saved as default (which overwrites the defaults file), the defaults file will then still contain values from a previous run.

The run-time inputs required from the user are outlined in Fig. 37. After providing the names of the data files and the water depth, the user must provide the necessary information to model the illumination conditions. The sections of the code that compute the illumination conditions were taken directly from BMC3D.

Outputs from `shade_c` include `Lu_err.dat`, which reports the shading error ε , original L_u^m , and corrected L_u , each as a function of wavelength, and `I_det.txt`, which contains detailed information of the input sky conditions for the run. Currently a `debug.dat` file is also generated when `shade_c` is run to capture additional information about the simulation.

We have also written a Matlab version of `shade_c`. This currently has fewer options for atmospheric conditions, but has some other enhanced capabilities, including the option to directly use the analytical models rather than the numerical tables to calculate shading error.

Fig. 37 — Flow diagram for the use of the self-shading correction code, `shade_c.f`

4.2 Field Data Examples

Shown in Fig. 38 are example water and seafloor optical property measurements from Lee Stocking Island. Shown on the left are the water absorption and scattering coefficient values measured with an ac-9 instrument (WET Labs, Philomath, Oregon) [4]. On the right are representative bottom albedo spectra for seagrass and coral sands [4]. The corresponding self-shading error spectra for these two LSI bottom types are shown in Fig. 39. Included are results for the two bottom types, two Sun angles (20 deg and 40 deg), and four different water depths. All cases show significant shading error over some portion of the spectrum. As expected, the amount of self-shading is higher for 20 deg than for 40 deg and higher over seagrass than over coral sands.

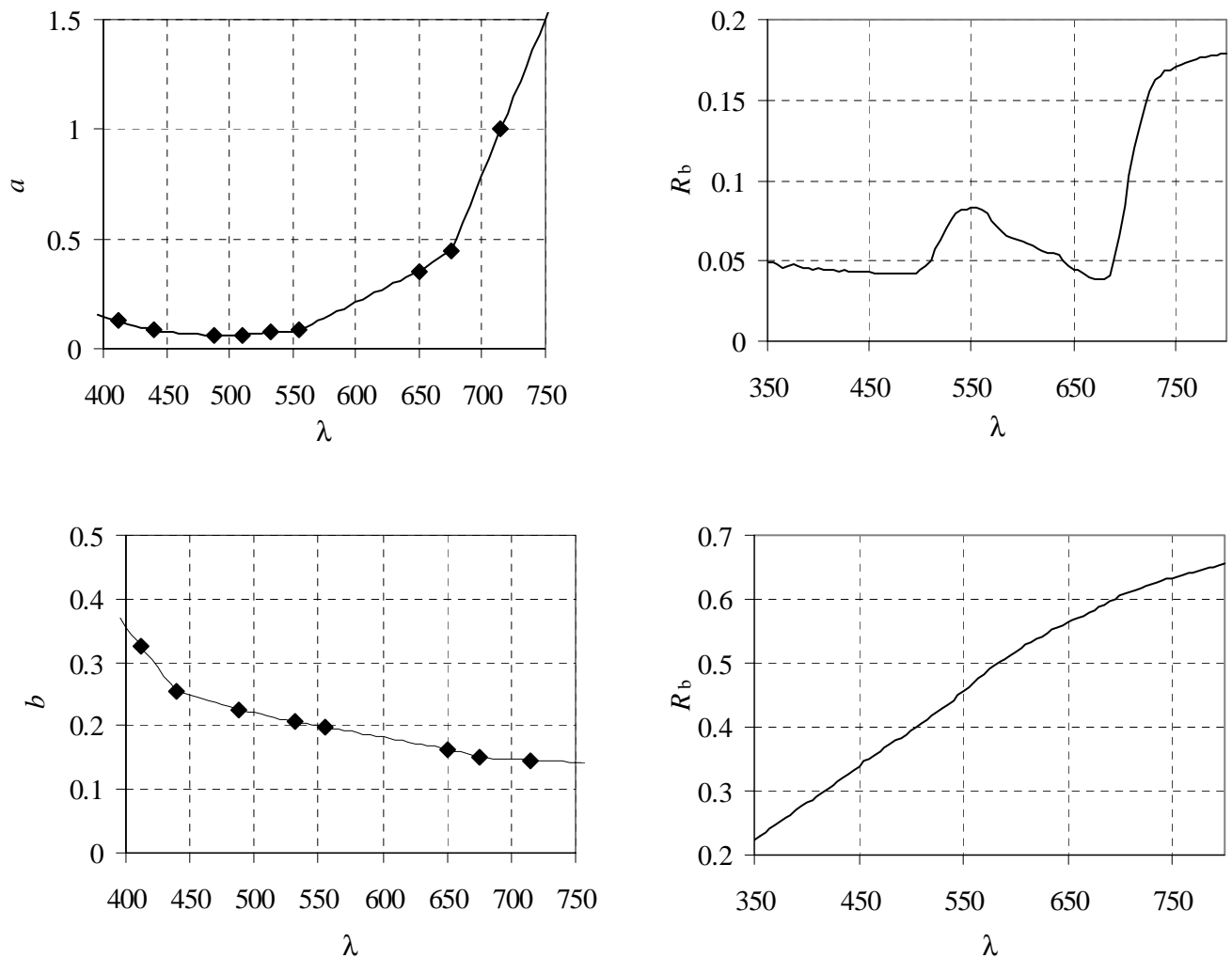


Fig. 38 — Example water and seafloor properties from LSI. The top R_b spectrum is for seagrass and the bottom R_b spectrum is for coral sands.

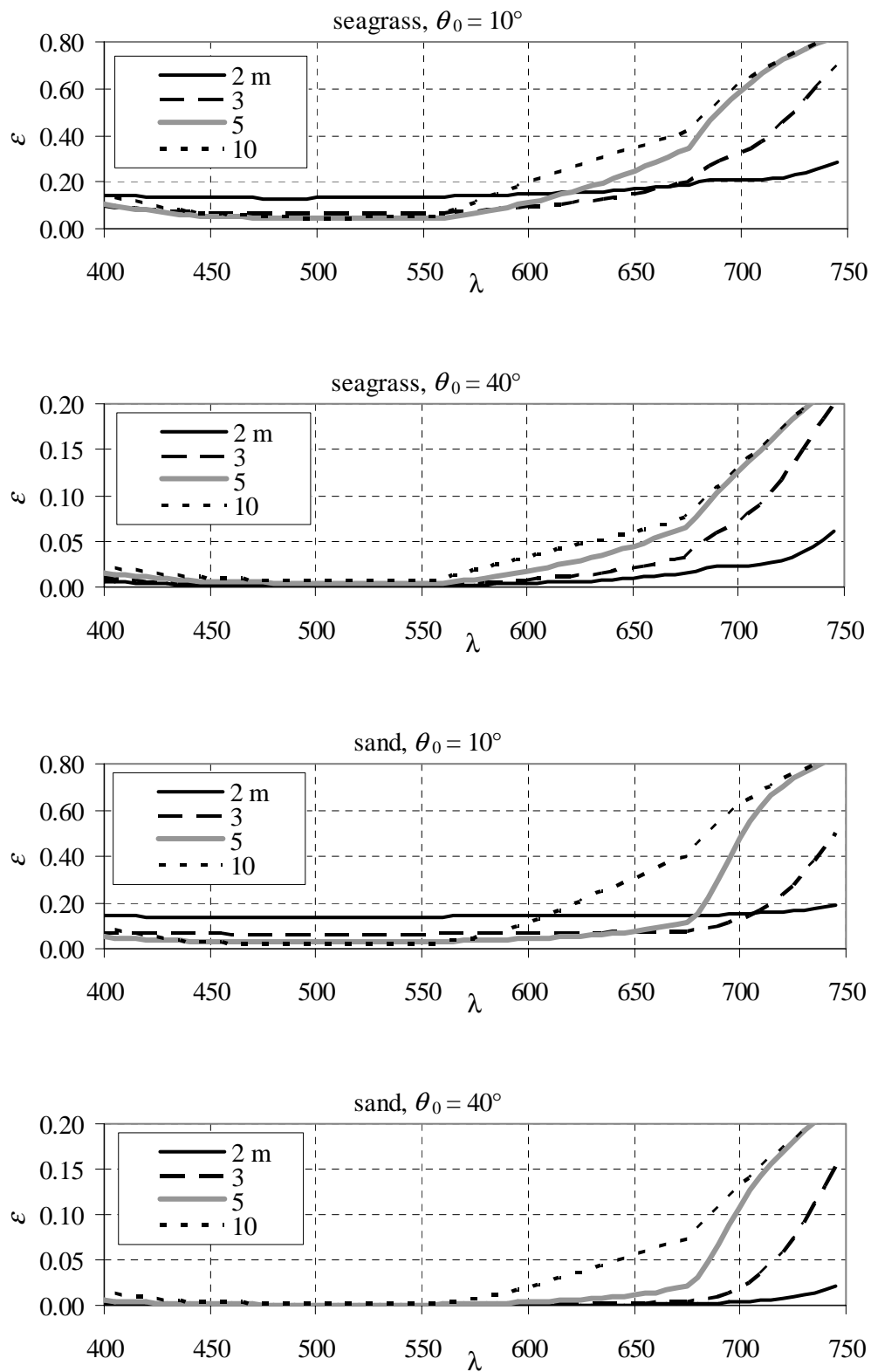


Fig. 39 — Hyper-TSRB self-shading error spectra for Lee Stocking Island, Bahamas, for a variety of water depths, bottom types, and Sun positions

5. CONCLUSIONS

Most commercially available instruments for measuring upwelling radiance are large enough that they suffer from significant self-shading error over at least some portion of the measured spectrum. The amount of error depends on instrument dimensions, sensor FOV, water optical properties (which are wavelength dependent), water depth, seafloor optical properties, Sun position, and atmospheric conditions.

Following the approach of Gordon and Ding [8], we derived an analytical model for the self-shading of a buoyed or nonbuoyed radiometer in optically deep waters [Eq. (21)]. This model performs well over a large range of typical conditions; however, it is inaccurate for very small solar zenith angles ($\theta_0 < 5$ deg) and for the combination of low solar zenith angles ($\theta_0 < 20$ deg) and high water absorption values ($a > 2 \text{ m}^{-1}$). The model takes neither sensor FOV nor water scattering into account; however, the effects of these parameters on shading in deep waters are usually small.

When a radiometer is optically close to the seafloor, the amount of self-shading is highly dependent on the sensor's FOV. We derived an analytical model for the self-shading of a buoyed or non-buoyed radiometer in very shallow water [Eq. (26)]. The shallow-water and deepwater models can be combined with Eqs. (28) and (29). The complete analytical model for any water depth is provided in Section 2.5.3.

The error values provided Eqs. (21) and Eq. (26) are for collimated light incident at a particular direction. To compute the overall error for particular illumination conditions, it is necessary to properly weigh the error values from all directions [e.g., Eq. (2) or Eq. (38)].

The analytical approximations of self-shading provide a practical tool for planning ocean optics experiments. Experiments should be planned so as to best avoid the collection of upwelling light measurements at times when self-shading is greatest. For a given suite of instrumentation, only the time of deployment (e.g., the position of the Sun) can be adjusted. However, problem conditions ($\theta < 10^\circ$) are rare and easily avoided. If an experiment cannot accommodate the time restrictions, then it may be necessary to invest in the development of smaller sensors or deployment packages for these experiments.

We modified a previously written Backward Monte Carlo program to numerically compute the self-shading of a buoyed or nonbuoyed radiometer as modeled by concentric solid cylinders. The radii and heights of the shading cylinders and the angular-dependent response function of the sensor are all easily adjusted. The results of these numerical simulations can be used to validate the analytical model for a particular instrument or to build a semianalytical model for cases where the analytical model is not appropriate.

If a radiometer is to be used in highly turbid waters and at relatively small solar zenith angles, we recommend that a semianalytical model be constructed that uses Monte Carlo results for optically deep water in place of Eq. (21). Because it is not necessary to vary water depth or bottom albedo in these computations, the number of simulations required is reasonable. The use of these numerical results introduces the proper dependence on water scattering and makes it possible to correct measurements at small solar zenith angle and higher water turbidity. Equations (26) and (28) can still be used to mesh together the deepwater and shallow-water shading predictions.

We have written a computer program that applies self-shading corrections to upwelling radiance spectra. The program itself is applicable to any instrument; however, one must supply the appropriate data tables for the instrument being corrected. The data tables can be generated from the analytical model, from Monte Carlo simulations, or from both. The program reads in data tables of a , b , and L_u ,

interpolates the data tables to obtain shading error for several different angular directions, and then uses input for Sun position and atmospheric conditions to compute the overall shading error.

The motivation of this research was to quantify self-shading for the Hyper-TSRB in shallow waters in order to correct data collected near Lee Stocking Island, Bahamas. We have constructed the data tables required by our correction code and can now easily correct any data taken with a Hyper-TSRB. The models and tools we developed for this task now provide us with the ability to predict self-shading errors for many other optical radiometers.

6. ACKNOWLEDGMENTS

This work was supported by the U.S. Office of Naval Research.

REFERENCES

1. C.O. Davis, J. Bowles, R.A. Leathers, D. Korwan, T.V. Downes, W.A. Snyder, W.J. Rhea, W. Chen, J. Fisher, and P. Bissett, "Ocean PHILLS Hyperspectral Imager: Design, Characterization, and Calibration," *Optics Express* **10**, 210-221, 2002.
2. R.A. Leathers, T.V. Downes, W.A. Snyder, J.H. Bowles, C.O. Davis, M.E. Kappus, M.A. Carney, W. Chen, D. Korwan, M.J. Montes, and W.J. Rhea, "Ocean PHILLS Data Collection and Processing: May 2000 Deployment, Lee Stocking Island, Bahamas," NRL/FR/7212--02-10,010, May 2002.
3. Coastal Benthic Optical Properties (CoBOP) program, 1998-2002, U.S. Office of Naval Research. <http://www.psicorp.com/cobop/cobop.html>.
4. H.M. Dierssen, R.C. Zimmerman, R.A. Leathers, T.V. Downes, and C.O. Davis, "Ocean Color Remote Sensing of Seagrass and Bathymetry in the Bahamas Banks by High-resolution Airborne Imagery," *Limnol. Oceanogr.* **48**, 444-455, 2003.
5. E.M. Louchard, R.P. Reid, F.C. Stephens, C.O. Davis, R.A. Leathers, and T.V. Downes, "Optical Remote Sensing of Benthic Habitats and Bathymetry in Coastal Environments at Lee Stocking Island, Bahamas: A Comparative Spectral Classification Approach," *Limnol. Oceanogr.* **48**, 511-521, 2003.
6. E.M. Louchard, R.P. Reid, C.F. Stephens, C.O. Davis, R.A. Leathers, T.V. Downes, and R. Maffione, "Derivative Analysis of Absorption Features in Hyperspectral Remote Sensing Data of Carbonate Sediments," *Optics Express* **10**, 1573-1584, 2002.
7. K.L. Carder, C.C. Liu, Z.P. Lee, D.C. English, J. Patten, F.R. Chen, J.E. Ivey, and C.O. Davis, "Illumination and Turbidity Effects on Observing Faceted Bottom Elements with Uniform Lambertian Albedos," *Limnol. Oceanogr.* **48**, 355-363, 2003.
8. H. Gordon and K. Ding, "Self-shading of In-water Optical Instruments," *Limnol. Oceanogr.* **37**, 491-500, 1992.
9. D.R. Lyzenga, "Remote Sensing of Bottom Reflectance and Water Attenuation Parameters in Shallow Water Using Aircraft and Landsat Data," *Int. J. Remote Sensing* **2**, 71-82, 1981.

10. H.R. Gordon, O.B. Brown, R.H. Evans, J.W. Brown, R.C. Smith, K.S. Baker, and D.K. Clark, "A Semianalytic Radiance Model of Ocean Color," *J. Geophys. Res.* **93**, 10909-10924, 1988.
11. J.E. O'Reilley, S. Maritorena, B.G. Mitchell, D.A. Siegel, K.L. Carder, S.A. Garver, M. Kahru, and C. McClain, "Ocean Color Chlorophyll Algorithms for SeaWiFS," *J. Geophys. Res.* **103**, 24937-24953, 1998.
12. D.R. Lyzenga, "Passive Remote Sensing Techniques for Mapping Water Depth and Bottom Features," *Appl. Opt.* **17**, 379-383, 1978.
13. M. Kahru and B.G. Mitchell, "Evaluation of Instrument Self-shading and Environmental Errors on Ocean Color Algorithms," Ocean Optics XIV Conference, Kona, Hawaii, 1998.
14. G. Zibordi and G.M. Ferrari, "Instrument Self-shading in Underwater Optical Measurements: Experimental Data," *Appl. Opt.* **34** (15), 2750-2754, 1995.
15. E. Aas and B. Korsbø, "Self-shading Effect by Radiance Meters on Upward Radiance Observed in Coastal Waters," *Limnol. Oceanogr.* **42** (5), 974-980, 1997.
16. J. Piskozub, A.R. Weeks, J.N. Schwarz, and I.S. Robinson, "Self-shading of Upwelling Irradiance for an Instrument with Sensors on a Sidearm," *Appl. Opt.* **39**, 1872-1878, 2000.
17. J.P. Doyle, "3D Instrument Self-shading Effects on In-water Multi-directional Radiance Measurements," Ocean Optics XV Conference, Monaco, 2000.
18. J.L. Mueller and G.S. Fargion, "Ocean Optics Protocols for Satellite Ocean Color Sensor Validation, Revision 3," NASA Tech. Memo. 210004, NASA Goddard Space Flight Center, Greenbelt, Maryland, 2002.
19. C.D. Mobley, *Light and Water* (Academic Press, New York, 1994).
20. R.M. Pope and E.S. Fry, "Absorption Spectrum (380-700 nm) of Pure Water. II. Integrating Cavity Measurements," *Appl. Opt.* **36**, 8710-8723, 1997.
21. Long-term Ecosystem Observatory (LEO), <http://marine.rutgers.edu/mrs/LEO/LEO15.html>.
22. K.S. Baker and R.C. Smith, "Irradiance Transmittance through the Air-water Interface," *Ocean Optics X*, R. W. Spinrad, ed., *Proc. SPIE* **1302**, 556-565, 1990.
23. C.D. Mobley, B. Gentili, H.R. Gordon, Z. Jin, G.W. Kattawar, A. Morel, P. Reinersman, K. Stamnes, and R.H. Stavn. "Comparison of Numerical Models for Computing Underwater Light Fields," *Appl. Opt.* **32**, 7484-7504, 1993.
24. H.R. Gordon, "Ship Perturbation of Irradiance Measurements at Sea. 1. Monte-Carlo Simulations," *Appl. Opt.* **24**, 4172-4182, 1985.
25. C.D. Mobley and L.K. Sundman, "Effects of Optically Shallow Bottoms on Upwelling Radiances: Inhomogeneous and Soping Bottoms," *Limnol. Oceanogr.* **48**, 329-336, 2003.
26. W.W. Gregg and K.L. Carder, "A Simple Spectral Solar Irradiance Model for Cloudless Maritime Atmospheres," *Limnol. Oceanogr.* **35**, 1657-1675, 1990.

27. F. Kasten and G. Czeplak, "Solar and Terrestrial-radiation Dependent on the Amount and Type of Cloud," *Solar Energy* **24**, 177-189, 1980.
28. A.W. Harrison and C.A. Coombes, "An Opaque Cloud Cover Model of Sky Short Wavelength Radiance," *Solar Energy* **41**, 387-392, 1988.
29. M.T. Hagan, H.B. Demuth, and M.H. Beale, *Neural Network Design* (PWS Publishing, Boston, 1996).
30. G.R. Fournier and J.L. Forand, "Analytic Phase Function for Ocean Water," in *Ocean Optics XII*, J.S. Jaffe, ed., *Proc. SPIE* **2258**, 194-201, 1994.
31. T J. Petzold, "Volume Scattering Functions for Selected Ocean Waters," SIO Ref 72-78 (Scripps Institution of Oceanography, La Jolla, CA, 1972).
32. R.A. Leathers, T.V. Downes, and C.D. Mobley, "Self-shading Correction for Upwelling Sea-surface Radiance Measurements Made with Buoyed Instruments," *Optics Express* **8**, 561-570, 2001.